Thesis for the degree of Licentiate of Engineering

Experimental Aerothermal Study on Internal Jet Engine Structures

Isak Jonsson

Department of Mechanics and Maritime Sciences
CHALMERS UNIVERSITY OF TECHNOLOGY
Göteborg, Sweden 2020

Experimental Aerothermal Study on Internal Jet Engine Structures
ISAK JONSSON

Licentiatavhandlingar vid Chalmers tekniska högskola
Technical report No. 2020:12

Department of Mechanics and Maritime Sciences
Chalmers University of Technology
SE–412 96 Göteborg, Sweden
Telephone + 46 (0) 31 – 772 5079

Cover: Surface temperature on the suction side of a outlet guide vane in a turbine rear structure.

Typeset by the author using LaTeX.

Printed by Chalmers Reproservice
Göteborg, Sweden 2020

"Design is an iterative process. The necessary number of iterations is one more than the number you have currently done. This is true at any point in time." - Akin's Laws of Spacecraft Design

Abstract

Experimental Aerothermal Study on Internal Jet Engine Structure
Thesis for the degree of Licentiate of Engineering in Thermo and Fluid Dynamics
ISAK JONSSON
Department of Applied Mechanics
Division of Fluid Dynamics
Chalmers University of Technology

For commercial aviation, one potential gain in efficiency can be found in the jet engine auxiliary modules, such as internal jet engine components. These components have historically largely been overlooked, prioritising units such as turbines or compressors. The publically available information for these auxiliary units is therefore relatively sparse even though they can enable substantial weight reduction and novel synergistic integration. The continuously increased fidelity of modern numerical tools poses a dilemma to the experimentalist. Higher accuracy and resolution are sought, but the accuracy of the experimentalist tools has stagnated.

This thesis summarises instrumentation implemented methods in the Turbine Rear Structure(TRS). For the multi-hole probe and heat transfer measurement via IR-thermography a comprehensive uncertainty analysis and error mitigations are presented.

The work presents a relatively high accuracy of 4% to 6% for the performed heat transfer studies on the outlet guide vane in the TRS. The presented implementation of the multi-hole probe in the TRS provides up to twice as high accuracy compared to conventional installation. Both approaches are general with few geometrical limitations and can be implemented on studies with similar ambient conditions.

Two different Reynolds numbers, several flow-coefficients and three different surface roughness numbers have been investigated and novel results regarding transition location, streamline, heat transfer and loss distribution are presented in the attached papers.

Aerothermal, experimental, multi-hole probe, IR-thermography, transition, Turbine Rear Structure, Intermediate Compressor Duct

Acknowledgments

As my work in the lab has been connected to numerous projects in different fields there are too many people to mention who I would like to thank for thier great company, help and interesting discussions. In the interest of keeping this thesis as short and consistent as possible, I hereby give my gratitude to all of you. If you feel this credit belongs to you, it probably does. There are, however, some individuals that are directly connected to this thesis and cannot be left out with a clear conscience.

First is my very knowledgeable supervisor Professor Valery Chernoray who has done his best to steer me away from ill-suited decisions since my first day in the lab too many years ago. Professor Tomas Grönsted and Docent Carlos Xisto should also be mentioned for their great support and trust in me in our ongoing venture in ENABLEH2. Ph.D Borja Rojo for enduring me during the intensive but interesting period of finalising the LPT-OGV rig. I'm also honoured to work with such great colleagues and collaborators that are heavily represented but far from exclusive in the Division of Fluid Dynamic at Chalmers and at GKN aerospace.

Finally, I would like to thank my family and Carmen for just being great.

Work in this thesis was financially supported by: i) VINNOA in the Swedish National Aviation Engineering Research Programme(NFFP) through project AT3E, Moststrom and AROS. ii) The EU commission in the CleanSky2 programme via project EATEEM and ENABLE-H2. iii) The department of the Department of Applied Mechanics. iv) GKN Aerospace Trollhättan. v) The Chalmers Laboratory of Fluids and Thermal Science.

Isak Jonsson
Göteborg, June 2020

List of Publications

This thesis is based on the following appended papers & proceedings:

Paper 1 Isak Jonsson, Valery Chernoray, Borja Rojo. *Surface Roughness Impact On Secondary Flow And Losses in a Turbine Exhaust Casing*, Proceedings of ASME Turbo Expo 2018, GT2018-75541.

Paper 2 Isak Jonsson, Valery Chernoray, Radeesh Dhanasegaran. *Infrared Thermography Investigation of Heat Transfer on Outlet Guide Vanes in a Engine Exit Module*, Submitted to IJTP (2020).

Paper 3 Srikanth Deshpande, Isak Jonsson, Valery Chernoray. *Effect of Surface Roughness on Aerodynamic Performance of Turbine Rear Structure*, Proceedings of ASME Turbo Expo 2019, GT2019-90472.

Paper 4 Isak Jonsson, Srikanth Deshpande, Valery Chernoray, Oskar Thulin, Jonas Larsson *Numerical and Experimental Study off Transition in an Engine Exit Module* ASME Turbo Expo 2020, GT2020-14990.

Nomenclature

Abbreviations

ADP – At Design Point
DIT – Differential Infrared Thermography
FFT – Fast Fourier Transform
FSD – Full Scale Deflection
HEX – Heat Exchanger
HPC – High-Pressure Compressor
HTC – Heat Transfer Coefficient
ICD – Intermediate Compressor Duct
IGV – Inlet Guide Vane
LPC – Low-Pressure Compressor
LPT – Low-Pressure Turbine
MCS – Monte Carlo Simulation
MHP – Multi-hole Probe
NGV – Nozzle Guide Vanes
OGV – Outlet Guide Vanes
PIV – Particle Imaging Velocimetry
RMA – Reflective Marker Array
RMS – Root Mean Square
SFS – Sliding Frame Subtraction
SLA – Stereolithography
SLS – Strained Layer Superlattice
SST – Menter's Shear Stress Transport
TRS – Turbine Rear Structure

Latin

A – Area
b_1 – MHP angle coefficient
b_2 – MHP angle coefficient
A_t – MHP Total Pressure coefficient
A_s – MHP Static Pressure coefficient
C_p – Pressure Coefficient

C_{p0} – Total Pressure Coefficient
h – Heat transfer Coefficient
K – Acceleration parameter
– Kelvin (°)
k_s – Sand-grain roughness
$k_{s,h}$ – Sand-grain roughness roughness Height
k_s^+ – Equivalent Sand-grain roughness
k – Thermal Conductivity
P^* – Normalised Total Pressure
U – Velocity
R – Reading of value
Re – Reynolds Number
Re_θ – Momentum Thickness Reynolds Number
R_a – Arithmetical mean deviation, surface roughness
R_q – Root mean squared, surface roughness
R_y – Maximum Height of the Profile,surface roughness
Rsk – Skewness, surface roughness
Tu – Turbulence Intensity
T – Temperature
t – Thickness
q – Dynamic Pressure
q_c – Quasi Dynamic Pressure
q'' – Heat flux (w/m^2)
P_s – Static Pressure
P_t – Total Pressure
P_i – Pressure of port or location
– Port perceiving highest pressure
P_{amb} – Absolute Pressure

Greek

α – Angle in XZ-plane for the MHP
– The swirl in the TRS
– Thermal Expansion Coefficient
β – Angle in XY-plane for the MHP
ϕ – Roll Angle
– Flow Coefficient
θ – Cone Angle
– Load Coefficient
δ_v – Viscus Sub-layer Thickness
δ – Individual Error
– Momentum Thickness
ε – Propagated/total error
– Emissivity

ρ – Density
σ – Standard Deviation
– Stefan-Boltzmann Constant

Subscript

ref – Relative to measurement point
t – Onset of laminar-turbulent transition

Superscripts

$+$ – Port perceiving the highest Pressure
$-$ – Port perceiving the lowest Pressure
$\bar{\xi}$ – Area Average
$\tilde{\xi}$ – Mass flow Average
$\hat{\xi}$ – Time Average

Contents

Part I

Introductory chapters

Chapter 1

Introduction

Commercial aviation engines are truly marvellous machines. They consist of millions of lightweight parts, rotating at thousands of RPM and for some components, operate at gas temperatures above the melting point. This is achieved while maintaining long-term reliable operation, high thermal efficiency and high power density. Furthermore, there is a demand for higher power density and reduced component losses, both from the industry and from governmental regulations. As the fidelity of the individual components approaches the theoretical maximum, the effort to gain performance benefits becomes even more challenging for the designer.

Arguably, many of the advances in engine performance can be attributed to advances in numerical tools. The exponential growth of computational power has enabled the designer to use more advanced models and higher numerical discretisation at an ever more cost-effective price. The fidelity of the numerical methods has reached such a level that much of the iterative work that was conducted experimentally 30 years ago is now performed using simulations. Today's experimental work primarily focuses on verification or detailed studies outside or in the outer fringes of the numerical tools' capabilities. The value of the experimental work is unquestioned. However, as the fidelity of the numerical tools increases the experimentalist has become hard-pressed to measure with sufficient resolution and accuracy.

One of the main disadvantages for the experimentalist is that the accuracy of experimental devices does not follow the same steady exponential growth as computational power. The development of devices and measurement techniques is significantly more sporadic, with sudden leaps as new technology emerges. Some examples of such leaps are the commercial use of the piezoresistive pressure sensors in the late 1950s, the introduction of an infrared camera technique using Strained Layer Superlattice(SLS) by FLIR$^{\mathrm{TM}}$ and the modern introduction of Particle Image Velocimetry(PIV) in the 1980s.

Since the experimental instrumentation accuracy cannot be expected to increase at the same rate as the computational power, the experimentalist cannot simply buy better devices to achieve higher quality. This issue will be principal throughout this thesis in order is to improve measurement techniques for aerothermal studies in internal jet engine structures. The majority of the work is done by uncertainty mitigation and holistic engineering for measurement accuracy. The two main experimental methods studied in this work are flow studies via multi-hole probe pneumatic measurements and heat transfer studies using IR-thermography.

Multi-hole pneumatic probes are a well recognised and established measurement technique in both academic and industrial applications. It is used to measure flow velocities and pressures. The technique is based on the pressure difference between the ports on the probe tip. This work describes the state-of-the-art of this technique and some of the problems when implemented in low-loss high-dynamic pressure environment.

IR-thermography is a technique that utilises the infrared spectrum radiation to measure surface temperature. In this work, surface temperature measured with IR-thermography is used to measure surface heat transfer coefficient(HTC) by solving conjugate heat-transfer along a vane wall.

The two above measurement methods mentioned above have been or will be implemented on two internal jet engine structures, a turbine rear structure(TRS) and an intermediate compressor duct(ICD). A substantial amount of work was required to construct these facilities and operational conditions in which the measurement were or will be performed. However, most of the work related to design and instrumentation has not been included in this thesis. The design of the LPT-OGV test facility for evaluation of the TRS is comprehensivly covered by Perez et al. [40]. The low-pressure compressor facility to evaluate the ICD is under construction and will be briefly presented in this work.

1.1 Aim of the Study

The primary aim of this thesis is to study and develop methods to experimentally measure the aerothermal performance of engine structures and ducts in turbomachinery. This thesis principally focuses on the measurement techniques and not the construction of the necessary surrounding facility to achieve the appropriate operational conditions. However, an introduction of internal jet engine structures and key experimental challenges is presented.

Chapter 2

Internal Jet Engine Structures

This section acts as a general introduction to internal jet engine structures regarding their mechanical and aerodynamic usage in commercial jet engines. Many of the generalisations described below are valid for most practical real engine configurations. All aero surfaces designed by GKN are aimed at the facilities at Chalmers and do not represent any GKN product characteristics. The term internal jet engine structures refers to components that transfer a substantial mechanical load through the core gas path. The location of the ICD and TRS is illustrated in Fig. 2.1 using the schematics of a Rolls-Royce$^{\text{TM}}$Trent-1000 commercial jet engine. The ICD is one of the key components to transfer the mechanical load from the front bearing through the gas path, while the TRS carries the mechanical load from the rear bearing to the rear engine mount. Geometrically, the two components share some common traits. It can be noted that the ICD and TRS have larger and considerably fewer struts/vanes compared to the adjacent compressor or turbine stages. This is true for most engines, although the exact ratio varies. The struts in these components have a lower aspect ratio and a thicker chord to make them more structurally robust and to allow for power and miscellaneous routing to pass through. Some of these are oil hoses for bearing cooling, bleeding of compressed air, or shafts for electric power generation. From an aerodynamic point of view, there is a penalty with thicker vanes with increased wetted surface. Another aspect of using thicker vanes is that the number of vanes has to be reduced in order to avoid large blockage of the core flow.

The coverage of the auxiliary modules is limited in the publicly available literature. As the potential incremental gain of components such as turbine and compressors are declining, the development of the auxiliary systems is getting attracting an increased attention. This thesis focuses on the TRS and the ICD, which are two of the main components of the internal jet engine structures.

2.1 Aerodynamic Function of the Turbine Rear Structure

The TRS and ICD fulfil different aerodynamic functions in a commercial jet engine. To maximise thrust, the TRS is designed to remove residual swirl at the outlet

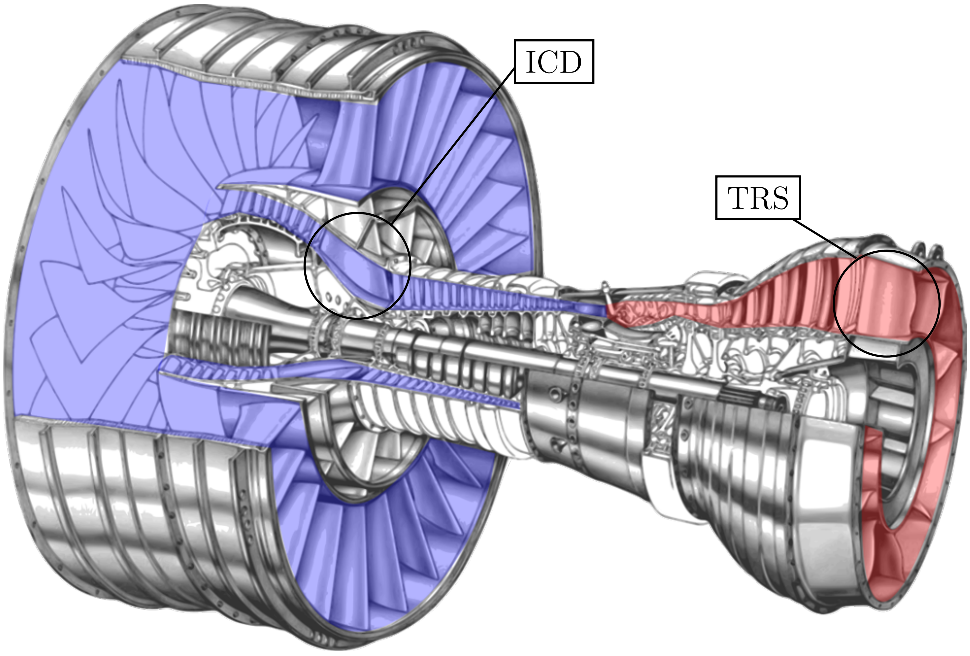

Figure 2.1: Commercial jet engine schematics with colour markup for hot and cold areas

of the last LPT stage. The design challenge is to deswirl the flow with minimum losses in the wide operational envelope of the TRS. The Reynolds number in a TRS ranges from 100,000 to 600,000, where several modes of transition can occur. Since the mode of transition has a significant impact on the turning performance of an airfoil, a TRS working adequately at sea level might lose several percentage points in performance at cruise conditions due to this effect alone.

The relatively large range in Reynolds number with altitude is primarily a consequence of density change. Relative pressure variations are directly related to ambient conditions which change by a factor of four from sea level to cruise altitude. On the other hand, the temperature varies substantially during a normal operational cycle. With the introduction of the geared and ultra-high by-pass engine concept, the operational window for the LPT is further expanded with larger ranges of LPT outlet swirl angles and temperatures. This will further challenge the designer of the TRS.

Figure 2.2a provides an isometric view of the TRS baseline geometry with the upstream LPT stage. The flow passes from left to right through the NGV and through the rotating LPT, before entering the TRS module. Seen from downstream, the rotor rotates clockwise while the midspan LPT outlet flow is angled counter clockwise. In this illustration, the suction side of the Outlet Guide Vane(OGV) is depicted, where the blue lines show topological streamlines at design condition. The blue shaded area shows the expansion of secondary flow structures from the leading edge saddle point, defined as a closed corner separation by Taylor in [46]. The green shaded line shows the observed locations of laminar-turbulent transition, and the spanwise arrows show the traverse pressure gradient. The two location of measurement are illustrated in Fig. 2.2a using a green and a red plane for inlet

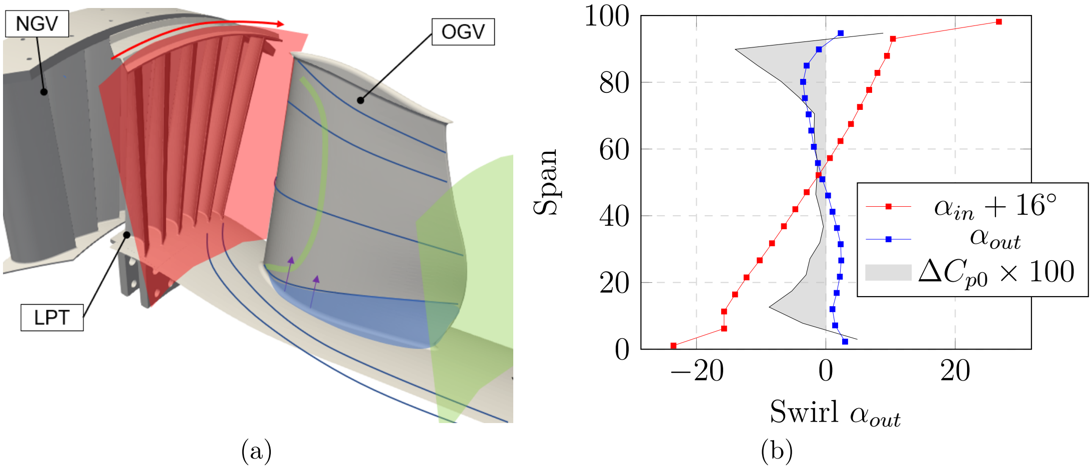

(a) (b)

Figure 2.2: Topology of the TRS from experimental studies, with streamlines in blue solid lines, transition location in green lines, and inlet and outlet in red and green planes respectively. General inlet and outlet flow angles at design point of the TRS together with the normalised loss distribution

and outlet measurement respectively. Figure 2.2b shows the average spanwise swirl distribution at the inlet and outlet planes. It can be observed that the average inlet swirl angle distribution is more profound near the hub with a higher incidence near the hub and a negative incidence above 90% span. It should be noted that the inlet swirl α_{in} has been shifted 16 degrees towards centre. The average outlet swirl angle is closer to zero with $\pm 1 - 3°$ variation across the full span. The spanwise loss distribution is shown as a grey shaded area with low losses at midspan and a substantial difference near the walls. In order to achieve an axial outlet flow, the hub region of the OGV is forced to performe substantially more deswirling compared to the rest of the vane. This is typical for stators both in turbines and compressors and the same topological terminology can be used for the secondary flow structures which have been concisely summarised by Harvey [22]. It should be noted that the OGV has a variable thickness, stacking angle and chord length and is far from a generic two-dimensional stacked airfoil. At design conditions, the high blade loading near the hub causes favourable conditions for the growth of the low momentum secondary stream tubes, near wall separations and cross-flow structures. These secondary flow structures comprise a large part of the component overall losses. This can be seen in the spanwise averaged loss distribution shown in Fig. 2.2b, with the large spanwise losses below 25% span. Above 80% span a large pressure drop can also be observed. This is partly caused due to the mixing of the LPT tip leakage flow and partly due to secondary flow losses. As the tip leakage is not measured at the inlet, the top losses are largely unknown. Only at very few inlet swirl angles do friction losses comprise a major part of the total losses, because when inlet angles are reduced, other secondary flow structures near the shroud become dominant. Due to the importance of losses in the lower spanwise area the work in this thesis focuses on this region and features that affect it.

Because the TRS operates in the hot core gas path, the thermal loads need in order to maintain mechanical integrity. One key challenge when predicting the thermal loads in a TRS is the convective heat transfer. This has been addressed in this work and is presented in Chapter 3 and Paper 3.

The design of the baseline TRS is complex and falls outside the scope of this work, with large variations in chord thickness, chord length and stacking angles to subsist with several competing flow structures within the TRS. The aerodynamic design of the NGV, LPT and TRS in this thesis was designed by GKN Aerospace.

Several previous studies of the TRS have been performed in a linear cascade where the large three-dimensional effect cannot be replicated. Hjärne published several aerodynamic studies of a midspan OGV in Chalmers linear cascade [23, 24, 25]. In the same facility Rojo [41] and Wang [50] performed heat transfer studies. Both numerical and experimental aeroacoustic studies have been performed at TU Graz using an annular TRS with Reynolds numbers up to 120.000 in Ref. [32, 45]. Before the inauguration of Chalmers' OGV-LPT facility there were no annual experimental studies in the public domain known to the author of a TRS at Reynolds numbers higher than 120.000.

2.2 Aerodynamic Function of the Intermediate Compressor Duct

In the ICD, the challenge is to efficiently guide the flow from the low-pressure compressor(LPC) to the high-pressure compressor(HPC) via a S-shaped duct with a minimal axial distance, i.e. as short as possible with a minimal pressure loss. Because the flow exiting the ICD enters the HPC, the outlet of the ICD must be compatible with the HPC. An isometric view of the studied ICD is provided in Fig. 2.3 with the core flow entering from the left. The outlet flow from the upstream LPC is deswirled by the OGV so the flow entering the ICD is nearly axial. In the duct there are struts that are transporting the mechanical loads through the gas path.

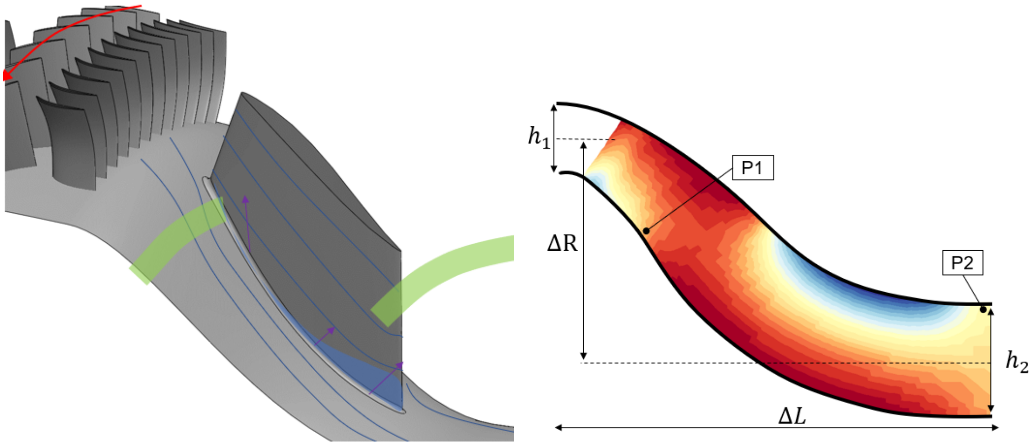

(a) Topology of an ICD using data from numerical studies

(b) C_p distribution and fundamental design parameters for the ICD

Figure 2.3: Schematic view of flow in the ICD(a) and a section of the pressure in the free-stream

At a fundamental level, as the length ΔL of the duct is reduced while keeping the radial distance ΔR constant, the limiting factor is the adverse pressure gradient that arises on the concave parts of the S-duct. This occurs at two locations, at the hub(P1) as the core flow is guided radially, and at the shroud, when the flow is again guided axially(P2). The adverse pressure gradient at the second point can be reduced by accelerating the flow in the later part of the duct, e.g. by reducing the cross section area $A_{out} \approx \pi h_2 r_2$ for example. The abovementioned parameters are common design parameters for the ICD.

The inlet flow to the duct is not uniform, with static and rotating wakes from the upstream compressor and OGVs. Britchford et al. [11] showed the importance of including upstream flow from the rotors as the boundary layer could be re-energised by the upstream rotor and a 21% shorter duct could be achieved. In the ICD there are large struts that, if all else beinging constant, will accelerate the flow and increase the pressure losses in the duct. This was experimentally investigated and demonstrated by Bailes [7]. Moreover, the duct is not a smooth pipe, as a bleed valve is commonly place somewhere along the shroudline, which disturbs the flow. Chen et al. [12] showed that by ejecting the boundary layer at the shroud, the low momentum boundary layer is removed and the losses in the duct are reduced. Walker [49] showed that a higher stability of the duct also could be achieved by ejecting the boundary layer from the duct at the hub.

Siggeirsson [17] showed that the upstream secondary flow structure from the OGV hub area can interact with the secondary flow structures from the struts with significant effects on the uniformity of the outlet flow.

Hence, in a real ICD the adverse pressure gradient is the key limiter, although with strong influences from the complex flow structures. The topological flow structures in the ICD are shown in Fig. 2.3, where the blue lines represent streamlines at design condition. The blue shaded area shows the expansion of secondary stream tubes from the leading edge saddle point. The green shaded areas show where adverse pressure gradients are expected to have a significant impact on the transition mode or separation. A horseshoe vortex occurs at the leading edge of the strut, both at the shroud and hub. Because the flow is decelerated near the hub, the hub vortex expansion is substantially larger than at the shroud. As demonstrated by Siggeirsson [17], this area is also sensitive to wake integration with upstream flow features such as OGV wakes.

2.3 Fundamental Similarities

Even though the aerodynamic purpose and design challenges of the two component are significant different, from an experimental point of view, the problems are largely similar and are listed below.

- The two structures are static and do not add any work to the core flow. Both are located in the vicinity of units adding or extracting a large amount of work to or from the core flow. This makes data normalisation challenging as extremely small fluctuations of the upstream unit will obscure certain flow features in the investigated unit.

- The high work units upstream cause complex three-dimensional inlet conditions with mixed end-wall boundary layer, stator and rotor wakes, swirl and strong pressure gradients with a significant effect for the flow features in the investigated unit.
- The high complexity and the high variations of the flow make it challenging to select a stable reference for normalisation and differential measurements.
- The ICD and the TRS have few low aspect ratio vanes located downstream, along with a relativity high blade count and aspect-ratio. This causes wake and secondary flows interaction that are very different from typical rotor-stator interaction where aspect-ratio, blade height and number are similar.
- Both components have critical areas where several modes of transition and separation might occur over the engine operation. As shown in Fig. 2.3a the primary location for the ICD is at the hub and shroud lines. For the TRS, illustrated in Fig. 2.2a, the critical area is on the suction side, especially near the hub.
- The low aspect ratio together with the strong traverse pressure gradient have a significant impact on the secondary flow, which in both cases is the main source of pressure losses in a large portion of the operational space.
- The thick vanes allow for certain instrumentation. An example of such instrumentation is the pressure taps that can be easily fitted in the thick chord. The measurement technique for high accurate heat flux measurements implemented for this work is significantly impeded by thin or rotating blades.
- There are no shocks present in either of the components, making incompressible studies feasible for both.

2.4 OGV-LPT Test Facility

This section elaborates on the characteristics and capabilities of the Chalmers OGV-LPT test facility. Further details about the facility are presented by Rojo in [40]. The Chalmers OGV-LPT test facility is an annular semi-closed 1.5 LPT stage test facility built to test the aerothermal performance of the TRS in various engine-representative flow conditions. The operational envelope of the facility in terms of Reynolds number and midspan inlet swirl variation is shown in Fig.2.4.

In the same figure some examples of aircraft engines are given in relation to their operational Reynolds number. As the Reynolds number increases the range of possible inlet swirl is limited by the LPT operation range in terms of rotational speed and torque. The red marker shows the conditions for which the facility was designed. Experiments from $\mathrm{r} \times 10^{=50.000}$ to $\mathrm{r} \times 10^{=465.000}$ have been performed. Tests at higher

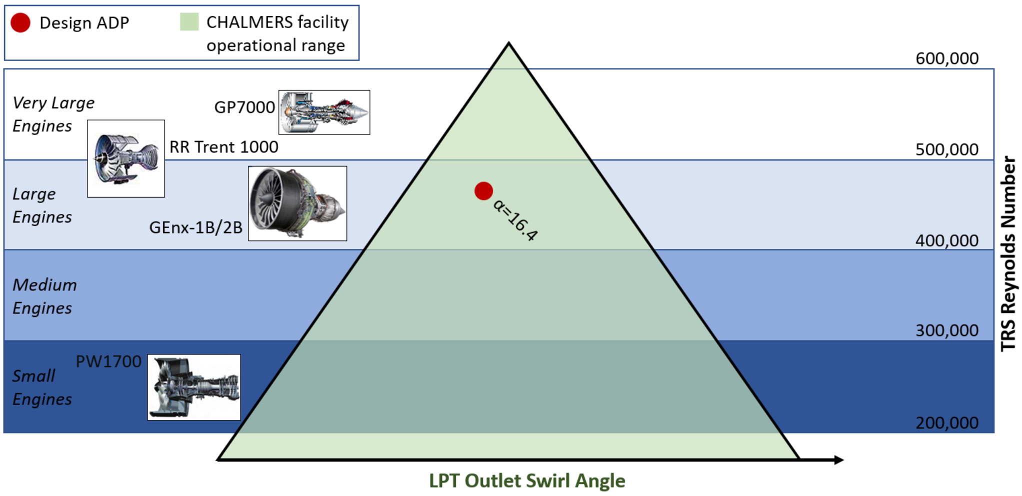

Figure 2.4: Chalmers OGV-LPT facility operational space

Reynolds numbers can also be performed with limited modifications. This allows the facility to create flows of representative conditions up to engines as large as the GP7000. Figure 2.5 shows the schematics of the facility. The facility is driven by a centrifugal fan. After the main flow is diffused and guided through corner ducts, a 2mx2m shim heat exchanger controls the main flow temperature using water from the central cooling system. Following this, in order to reduce non-uniformity flow structures, the flow is passed through a flow conditioner of stainless stainless steel screens and an aluminum honeycomb, following guidelines from [9, 21, 10]. The main flow is later accelerated through the contraction that was optimised by Rojo in [40].

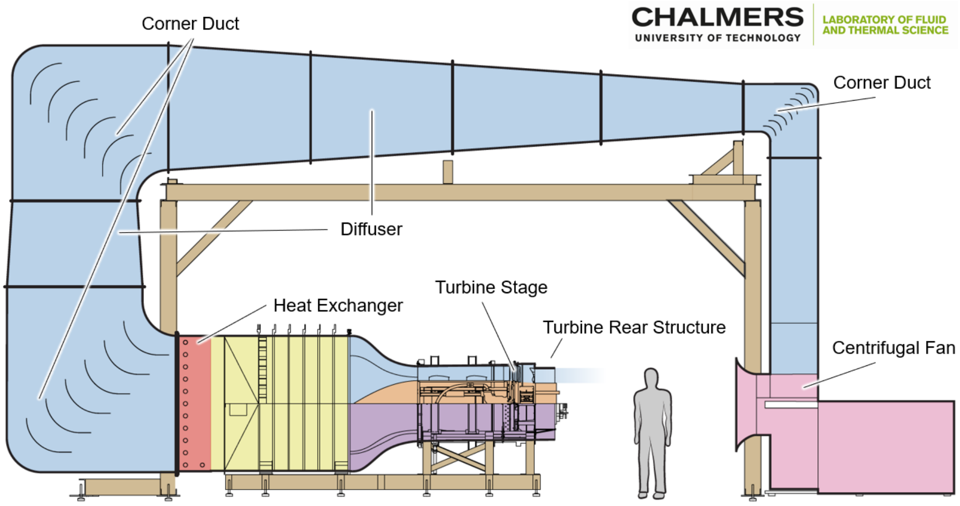

Figure 2.5: Chalmers OGV-LPT facility

The LPT is regulated by a hydraulic brake and extracts work from the main flow. After the single LPT stage, the main flow goes through the TRS module, which is directed towards the inlet of the centrifugal fan to recover the residual dynamic pressure. An isometric view of the TRS is shown in Fig. 2.6 including main instrumentation with a description and letter identifier. The TRS module

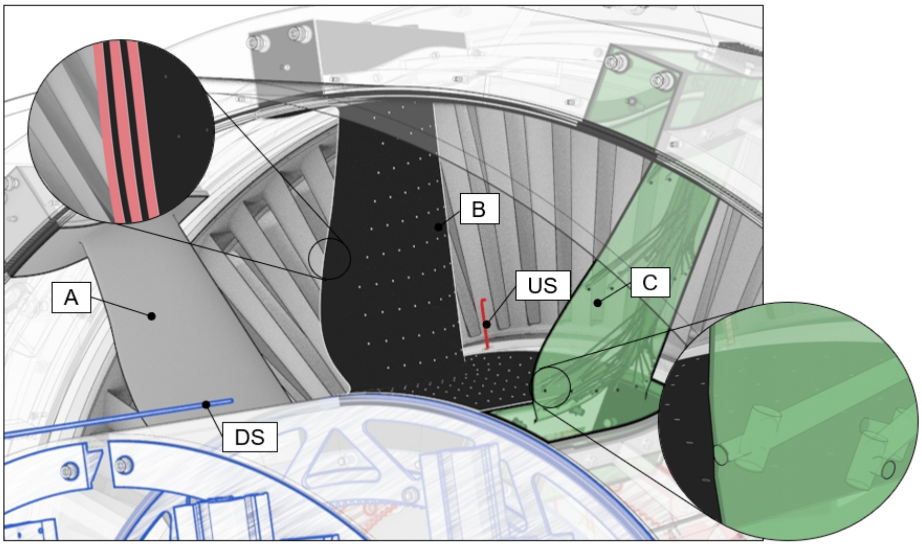

Figure 2.6: Isometric view of the test section with instrumentation location and generic data

is constructed to be modified and is therefore heavily modular. Each individual aero surface such as the OGV, shroud, P-flange pocket, purge-flow and hub can independently be exchanged or instrumented. Figure 2.6 shows three types of instrumented OGVs. Marked as B is the heated vane used for heat transfer (described in Sec. 4.2). Down to the left is a vane installed for flow visualisation (marked with A) and the one to the right is instrumented with pressure taps (marked with C). The instrumented OGVs are made by Stereolithography(SLA) and two detailed views of the internal water and pressure channels are shown. There are two traverse systems installed in the TRS, one upstream (marked with US) and one downstream of the OGVs (marked with DS). Both systems have a full 360-degree and channel radial range, the downstream traverse system is also capable of axial motion. The two traverse systems together enable a near full-volume 360 degree access of the TRS. In the test section there is a Prantl tube for measuring total and static pressure reference when normalising the data, as described in section 2.4.1.

Baseline instrumentation is two multi-hole probes, one mounted on each traverse system, and pressure taps installed on one or several OGVs. As the TRS module is modified often and substantially, the instrumentation varies. At the moment of writing, instrumentation such as hotwire, PIV, Flowvis, Iand R-Thermography has been successfully implemented.

More details about the design and construction of the facility can be found in [40].

2.4.1 Data Reduction in the TRS

During operation, the operator aims to achieve the representative Reynolds number and flow coefficient ϕ. These can be repeated with high confidence for typical variations of 0.2% to 0.3% in Reynolds number and 0.6% in flow coefficient ϕ. Since ambient conditions vary from day to day and during experiments, neither Fan RPM, turbine RPM, dynamic pressure nor total pressure in the TRS can be held constant. The measured pressure in the TRS needs to be normalised to enable comparison between different operational conditions in the TRS. One of the key challenges is the relatively high work extracted by the low-pressure turbine upstream. The area average pressure drop in the TRS is in the order of 0.2% of the turbine pressure drop. A tiny variation in the turbine work would therefore offset the whole mean flow variations. A larger cumulonimbus can cause a fluctuation in the order of 0.5% of turbine work when passing over the lab due to air density changes.

To cope with the variations of ambient conditions the permanently mounted Prantl probe is used as a reference. The probe provides flow field pressures during measurements which are used to normalise the pressures measured from the two multihole probe(MHP). For papers attached in this work the pressure coefficient Cp_0 and Cp are for this purpose and are defined in Eqs. (2.1) and (2.2) for total and static pressure coefficient representatively.

$$Cp_0 = \frac{p_{t,i} - P_{t,ref}}{q_{ref}} \tag{2.1}$$

$$Cp = \frac{p_i - P_{ref}}{q_{ref}} \tag{2.2}$$

In Paper 4 the total pressure coefficient P^* as defined in Eq. (2.3) is used as it is slightly more stable for pressure measurement when variations are small. The averaged reference pressure $\bar{P}_{t,ref}$ is used to scale for ambient fluctuations.

$$P^* = P_{t,i} \frac{\bar{P}_{t,ref}}{P_{t,ref}} \tag{2.3}$$

2.5 Low-Pressure Compressor Test Facility

The Low-Pressure Compressor Test Facility is yet to be commissioned. This section briefly presents the design philosophy and status of the facility at the date of writing. The facility is built as part of the ENABLEH2 project and is constructed in the Chalmers Laboratory of Fluids and Thermal Science. The main aim of the facility is to experimentally evaluate the ICDs ability to be synergistically utilised as a heat exchanger in cryogenic fueled engine concepts. The novelty in the component is to utilise the increased wetted area needed for heat transfer to aid the radial turning of the core flow in the ICD, thus enabling more aggressive ducts without large separations. The facility will first be evaluated using an engine-typical ICD's and later replaced with the novel synergistic ICD heat-exchanger concept.

The facility is a vertical annular 2.5-stage low-speed compressor rig, and the facility is built for continuous operation capable of running a wide operational range of Reynolds numbers and pressure ratios. The general layout of the facility can be seen in Fig. 2.7. A two-stage compressor provides all the input power to the facility. Operational conditions are achieved by restricting the flow with an upstream

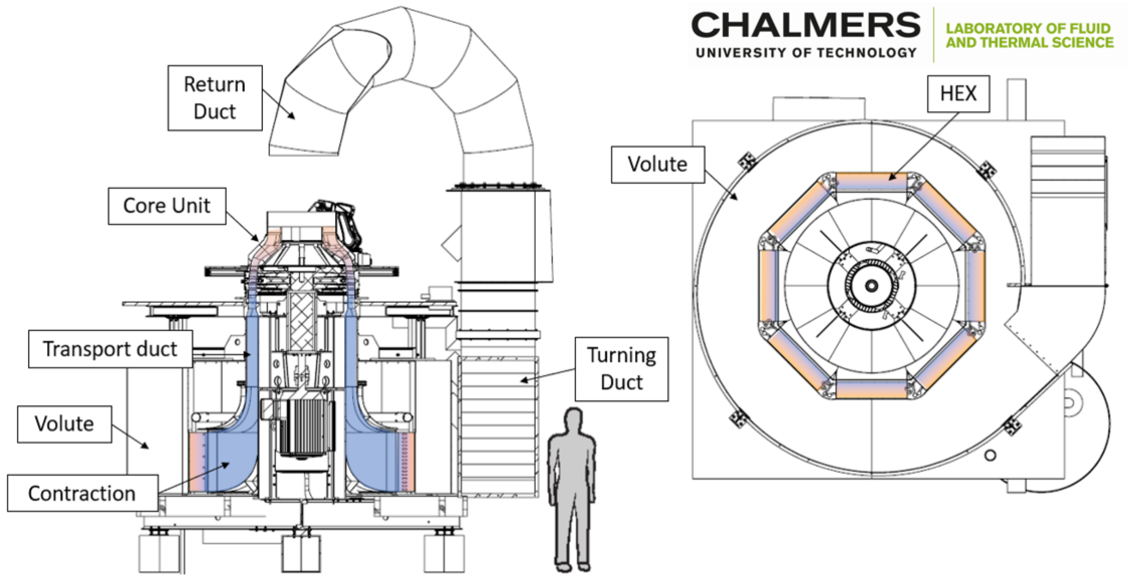

Figure 2.7: Schematics of Chalmers low-pressure compressor facility

flow restrictor and by regulating the input power to the compressor. The flow is conditioned for thermal and pressure uniformity in a combined volute and flow conditioner, between the restrictor and the compressor inlet. The ICD is mounted downstream of the two-stage compressor and the ICD outlet is the outlet of the facility. The flow is recirculated into the facility for thermal stability, but also to limit particle and noise mitigation between the laboratory and the facility.

The design of the facility can be divided into two groups, of which he first relates to the key core flow components, such as the compressor and the ICD. The secondary group is a grouping of all functions that support the first group, such as mechanical structure or cooling. A brief description of the main parts of the support system is provided below.

Power to the compressor is supplied by a modified low profile Bevi 3DL 280M2-4 three-phase industrial electric motor with a power output of 147kW at 1920 RPM. The size of the electric motor is decided by the output torque and a very limited the number of suitable options that would fit within the hub diameter were available. Electric motors provide excellent stability, accurate and simple control of the torque, and rational speed of the rotor. The motor is connected directly to the rotor shaft via a KTR Rotex 75 coupler.

Mass flow is primarily controlled by industrial jalousie dampers from Beverent Rasch and for fine adjustment three smaller by-pass Iris valves are used. Using industrial jalousie dampeners enables a simple control, however, the outlet flow from such a device is highly non-uniform and not suitable for cthe ompressor inlet without conditioning. Mass flow is measured over a contraction upstream of the inlet to the compressor. The contraction will be calibrated using two 600mm diameter external AMSE venturi as defined in ASME PTC 19.5 [3] that are connected to the inlet at commissioning.

Flow conditioning is needed to acquire uniform flow at the inlet to the compressor. The first step is to remove the large structures using stainless steel meshes and 100mm aluminium honeycomb structures. After the first step of flow conditioning, the flow enters a 90 degree corner duct guiding the flow in the azimuthal direction into a volute. The volute maintains a constant azimuthal velocity while the flow is guided radially through eight heat exchangers(HEX). The HEX serve two purposes, firstly, they keep the thermal balance in the facility as they are connected to the building central cooling system. Second, the HEX act as a flow conditioner reducing non-uniformity in the flow. The flow is accelerated after the HEX and guided from radial to axial direction. After the contraction, the flow is guided through a transport channel where it passes by structural NACA0018. After the transport channel, the flow is accelerated in a contraction with a contraction ratio of 0.85. Before entering the IGV, a turbulence screen is placed to increase turbulence levels and reduce residual non-uniformity arising from the NACA struts wakes.

The mechanical design of the support structures in the facility was primary aimed to simplify assembly and to enable easy access to the ICD and compressor. This is the main reason why the facility is constructed vertically and not horizontally. All parts were designed to have a safety factor above 3 for a five-year normal operation period. Different tools have been used to assess the design depending on the cost and risk factor. The structural integrity of the outer structures was assessed with fundamental hand calculations, while structures, such as the rotor were extensively simulated for both dynamic and static loads.

2.5.1 Core Unit Design Philosophy

The design of the compressor was balanced to maximise engine similitude and measurement accuracy. The design work can be divided into two main groups. One is intended to provide engine representative conditions to evaluate the ICD in, and the second is intended to maximise the quality of the data from the studies in the ICD. The compressor in the open access virtual engine VINK was used as starting engine reference. This engine is part of a collaboration project between Swedish universities and industry. The members of the project are the Chalmers University of Technology, KTH Royal Institute of Technology, Lund University, GKN Aerospace Sweden AB, and Swerea. The compressor power was scaled down for practical reasons such as available power, space in the lab, cooling sources, system pressure losses etc. A selection of these is presented below together with a short comment for each. When scaling the compressor power and speed, enabling accurate measurements was the key limitation that was prioritised above anything else.

Practical limitations at Chalmers Laboratory of Fluids and Thermal Science are summarised in Table 2.1. The power to the facility is primarily limited by the affordable and suitable cooling available from the central cooling system. Mass-flow and RPM scale to the size of the compressor but to avoid high compressible effects the tip speed was limited to 100 m/s. The floor could support two metric tonnes per square metre and a dew point of 13 $°C$ can be expected in the lab. The pressure transducers in the Chalmers Laboratory of Fluids and Thermal Science are in the range of 2.5 kPa to $5kPa$. Since probes are of a finite size, the resolution and number of points possible within a channel reduces in correspondence to the channel height. With probe sizes from 1mm to 3mm the number of measurement points in the spanwise direction is 25 to 80 with a minimum channel height of 80mm.

Table 2.1: Practical limitation in Chalmers Laboratory of Fluids and Thermal Science

-	-	Comment
Power	~130 kW	Amount of affordable cooling power available
RPM	2000	Tip speed ≈ 100 m/s
$\dot{m}$	20	Power and channel height
Weight (kg/m^2)	2000 kg/m^2	Max in the lab
Temperature	13° C	Typical dew point in the lab
Pressure Transducers	$2.5 - 5$ kPa	Available calibrator available
Channel Height	80mm$\geq h$	Probe blockage and resolution

Chapter 3

Laminar-turbulent Transition in the TRS

All but one of the attached papers are related to surface roughness or laminar-turbulent transition on an OGV. Therefore, a brief discussion about these two factors is included in this chapter. When discussing transition and roughness there are a few very useful parameters. The first is the momentum thickness Reynolds number Re_θ as defined in Eq. (3.1). The momentum thickness θ, free-stream velocity U_∞ and kinematic viscosity ν are is used to defined Re_θ.

$$Re_\theta = \frac{U_\infty \theta}{\nu} \tag{3.1}$$

Momentum thickness Reynolds number Re_θ is one of the main parameters when predicting transition on-set, both by correlations such as by Mayle [33] and Praisner [35] and in numerical tools such as in the SST $(\gamma - \theta)$ model [34]. A second important parameter is the acceleration coefficient K as defined by Eq. (3.2). The acceleration parameter is defined by the velocity at the edge of the boundary layer U with the partial derivative $\partial U/\partial s$ along a surface line s. The kinematic viscosity defined from properties in the free stream if not otherwise stated.

$$K_\theta = \frac{\nu}{U^2} \frac{\partial U}{\partial s} \tag{3.2}$$

The acceleration parameter is also commonly used in both transition models and correlation as it is useful to normalise effects from wall pressure gradient. The onset momentum thickness Reynolds number Re_{θ_t} is often confused when conceptualised. Here, the author prefers to define Re_{θ_t} by what it is not. It does not provide information about transition location or history of the boundary layer development. The perturbations in the boundary layer are reasonable to estimate to be scaled to the ambient flow velocity and momentum thickness and, at some point, should reach such a level that laminar-turbulent transition occurs. The Re_{θ_t} is often used to define the on-set of the laminar-turbulent transition and which is denoted with the subscript t. The acceleration parameter K_θ is significantly more common and simpler to relate to, a negative value represents an adverse pressure gradient and vice-versa. At very low values the flow separates, at very high values, you get relaminarisation or long streaks of laminar flow. The acceleration parameter is denoted with the subscript t at laminar-turbulent transition as with Re_{θ_t}.

Even though the flow in turbomachinery is highly turbulent and unsteady, the boundary layer can be both laminar or turbulent. Often the transition along the span of an airfoil is imagined to be two-dimensional, steady and single-directional, this is a dangerous oversimplification of the true flow. The transition process is stochastic, unsteady and bi-directional. The highly unsteady flow in turbomachinery from upstream rotors, combustors or other periodic structures can also introduce different modes of transition to occur at a different location at the same time. The mechanics behind different modes of transition and fundamental boundary layer theory are outside the scope of this chapter. The transition in gas turbine engines is comprehensively covered by Malye [33] and fundamental boundary layer theory by Schlichting [43].

There are several possible modes of transition between laminar and turbulent flow, namely natural transition, bypass transition, separation transition and reverse transition. Due to the high turbulence levels in turbomachinery, the laminar or natural transition rarely occurs. Bypass or separation transition has been experimentally observed on the suction side of the OGV in TRS. Relaminarisation or reverse transition can occur at areas with strong acceleration and can be found on the air pressure side in some components in turbomachinery. There are indications that this occurs in the TRS at certain locations on the pressure side but, to date, this have so far not been confirmed.

3.1 Turbulence Effects

Turbulence effects on the onset momentum thickness Reynolds number Re_{θ_t} are briefly discussed below. From a large set of empirical data, Mayle proposed that attached transition onset momentum thickness Reynolds number is primarily dependent on turbulence levels above 2% to 3%. For these conditions, momentum thickness Reynolds number at on-set could largely be described by using Eq (3.3). Turbulence intensity is given in percentage, $Tu = 100 \times U'/U$. This correlation corresponds well with the measurements in Paper 4 and is part of the foundation of the $(\gamma - \theta)$ SST model.

$$Re_{\theta_t} = 400 Tu^{5/8} \tag{3.3}$$

Other older correlations such as those from Abu-Ghannam [1] provide similar results as to Eq. (3.3) at conditions found in the TRS. A more recent correlation from Praisner [35] includes the integral length-scale to better predict the effect from turbulence. This model was attempted to be included in the discussion in Paper 4. Unfortunately, the method of measuring the integral length scale for that model requires a considerably more labour-intensive hot-wire signal post processing than was possible within the timeframe.

3.2 Surface Roughness Effects

The surface roughness affects the boundary layer development and transition on-set location. However, when experimentally working with surface roughness, the first problem is geometrical. From a fluid dynamic perspective, the geometrical sand-grain roughness k_s, sand-grain roughness height $k_{s,h}$ and the dimensionless friction factor f are commonly used. However, in practice the surface information provided is statistical, as defined by ISO-4287 [27]. The exact conversion from statistical ISO units such as R_a and R_y to geometrical sand grain roughness k_s is a much-debated subject. In Paper 3 a GKN in-house correlation was used to relate statistical values to surface roughness. The challenges to define a universal surface roughness to sand grain conversion are partly due to the effect of the surface is being heavily dependent on the thickness of the boundary layer.

The dependency of surface roughness effects on the boundary layer state can be framed by discussing the dimensionless surface roughness k_s^+. This is defined by the equivalent sand-grain roughness divided by the normalised to the viscus boundary layer thickness δ_v as shown in Eq. 3.4.

$$k_s^+ = \frac{k_s}{\delta_v} \qquad \underset{Smooth}{0 \leq k_s^+ \leq 5} \qquad \underset{Transitional}{5 \leq k_s^+ \leq 70} \qquad \underset{Rough}{70 \leq k_s^+} \tag{3.4}$$

The effect of the dimensionless surface roughness can be divided into three zones. Below a value of five k_s^+, the surface can be considered hydraulically smooth. At values with a dimensionless roughness parameter above 70 the surface can be considered fully rough as the average fluctuation has penetrated into the overlap region. In the area in between these two, in the transitional range, the surface topology has a large impact and the conversion from statistical to equivalent sand-grain roughness is challenging. One empirical model derived from a relatively large dataset of real surfaces is presented by Flack and Schultz [19] and is defined in Eq. (3.5). R_q is the RMS of perturbations and Rsk is the skewness as defined in ISO-4287. The skewness provides a measure off the direction of the surface variations. At a high skewness the majority of the perturbation extrudes into the flow and vice-versa.

$$k_s = 4.43R_q(1 + Rsk)^{1.37} \tag{3.5}$$

Assuming that surface roughness has been estimated correctly, the surface roughness effect on the laminar-turbulent transition on-set location can be estimated using the roughness parameter $\theta_t/k_{s,h}$. This parameter has been empirically correlated to the onset momentum thickness Reynolds number by using Eq. (3.6).

$$Re_{\theta_t} = 100 + 0.43exp(7 - 0.77\frac{k_{s,h}}{\theta_t}) \tag{3.6}$$

Equations (3.6) and (3.3) describe the effect from surface roughness and turbulence levels respectively and both are illustrated in Fig. 3.1. Figure 3.1 shows that for most turbulence levels present in the TRS, the sand-grain roughness height needs to be in the order of four times the size as the momentum thickness boundary layer θ to make an impact on the momentum thickness at transition onset. A very rough

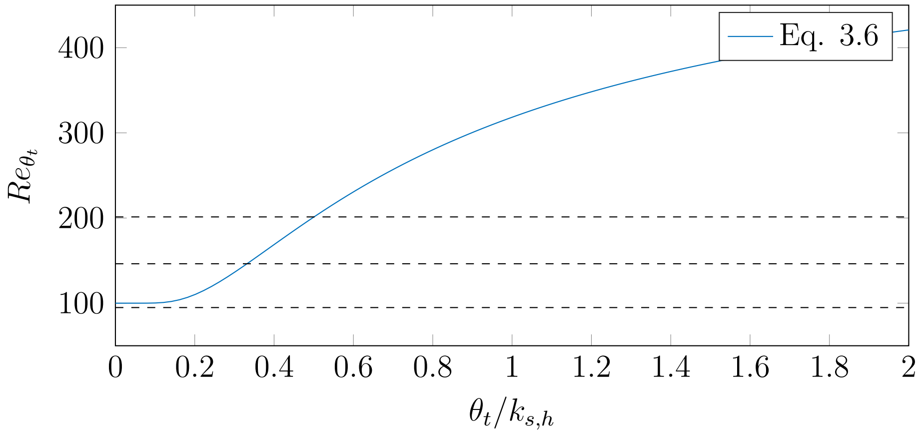

Figure 3.1: Turbulence and surface roughness effects on the transition onset momentum thickness Reynolds number Re_{θ_t}

surface was evaluated in Paper 1. Unfortunately, neither the surface skewness Rsk nor the θ_t was measured for the rougher surface. The peak perturbation height R_z was measured and could potentially be used as a conservative substation for $k_{s,h}$ but classical θ_t measurement with anemometry is a very tedious task and was not performed.

A large proportion of the effects found due to surface roughness in Paper 1 at high Reynolds number are still undocumented. Numerical studies in Paper 3 provide insight into the effect of surface roughness increases.

Chapter 4

Instrumentation and Measurements

This chapter presents the implementation and development of the multi-hole probe measurement technique and IR-thermography used in the appended papers. The fundamentals of each method will first be introduced, followed by the main challenges distinguished along the way and how these were mitigated. Only data related to experiments in the TRS are presented.

4.1 Multi-hole Probe

As the name suggests, the multi-hole probe is a probe with multiple holes in the tip. The shape of the tip or the number of holes varies depending on the type of probe, with the most common being five or seven holes with a conical or semispherical tip. The basic operation of a multihole probe is simple. As the probe is angled in the flowfield, the surface on the windward side will perceive a larger component of the stagnation pressure while the surface of leeward side will perceive a reduced static pressure. The holes in the probe capture this pressure difference, which is used to calculate the relative tip angle, the total, as well as the dynamic pressure of the flow.

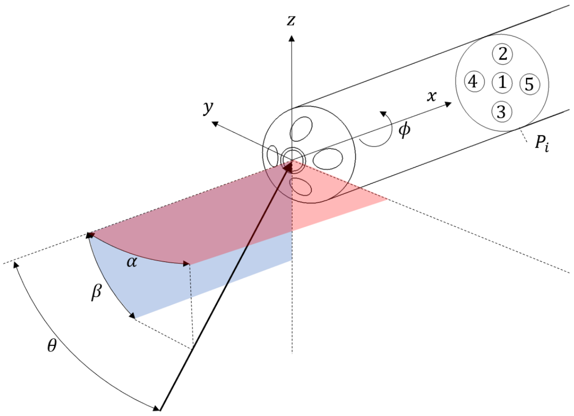

Figure 4.1: Probe coordinate systems and port indexing P_i for a five-hole probe

A typical five-hole probe is shown in Fig. 4.1 with port numbering and two interchangeable coordinate systems. The coordinate systems are based on the angle between the probe tip in relation to the flow. The (α - β) coordinate system is based on angle components in the $x-y$ and the $x-z$ planes in Cartesian coordinates. The flow is parallel to the probe when both α and β is zero. The second coordinate system ($\phi-\theta$) is based on the angle to and around the x-axis to define the flow relative to the probe tip. At parallel flow, the roll angle ϕ becomes undefined while the cone angle θ is zero. A multi-hole probe can be used in flow angles up to the point when substantial separation occurs on the leeward side of the probe. For a typical five-hole probe, this is in the vicinity of a cone angle of $45-60°$ depending on shape.

The probe can either be used in a nulling mode or a non-nulling mode. The non-nulling mode is also known as the calibrated mode. The nulling mode is based on finding a set ratio between the ports by orienting the probe in the flow. This can be suitable for two-dimensional flow but for highly three-dimensional flow, the orientation of the probe can be problematic. The traversing of the probe might not be possible due to space limitations or the number of degrees of freedom needed. The non-nulling mode can be made extremely sensitive to small flow angles.

The second mode is the non-nulling mode, where the probe is calibrated before measurement. This is achieved by traversing the probe in a known flow field for a wide set of flow angles. The pressure reading from the ports of the probe is reduced to dimensionless pressure coefficients and correlated to the known flow field. These coefficients are later used when the probe is inserted into an unknown flow field. This method is by far the most common implementation as probe size or imperfection have little effect and instrumentation is easier.

There are several formulations of dimensionless pressure coefficients. The most commonly used is the sectoring approach, as utilised by Barker and Crawford [8, 18, 15]. In this formulation, there are two definitions of the coefficients depending on the relative flow angle. Equation (4.1) is used when the centre port senses the highest pressure i.e. at flow at small cone angles. The second formulation, Eq. 4.2 shows the same coefficient for when one of the side ports senses the highest pressure, i.e. when the cone angles are large. This formulation is used in the Chalmers Laboratory of Fluids and Thermal Science and all attached papers.

$$angles\begin{cases} b_1 = \dfrac{p_2+p_4-p_5-p_3}{2q_c} \\ b_2 = \dfrac{p_5+p_2-p_3-p_4}{2q_c} \end{cases}, Pressure\begin{cases} A_t = \dfrac{p_1-p_{tot}}{q_c} \\ A_s = \dfrac{q_c}{p_{tot}-p_{stat}} \\ q_c = p_1 - \displaystyle\sum_{i=2}^{5}\frac{p_i}{4} \end{cases} \tag{4.1}$$

Subindex i is used for the port with the highest measured pressure, the adjacent side ports are super indexed with + and − for high- and low-pressure pressure sides, i.e. leeward and windward respectively.

$$angles\begin{cases} b_1 = \dfrac{p_i - p_1}{q_c} \\ b_2 = \dfrac{p_i^+ - p_i^-}{q_c} \end{cases}, Pressure\begin{cases} A_t = \dfrac{p_1 - p_{tot}}{q_c} \\ A_s = \dfrac{q_c}{p_{tot} - p_{stat}} \\ q_c = p_i - \dfrac{p_i^+ - p_i^-}{2} \end{cases} \tag{4.2}$$

The q_c is the quasi dynamic pressure which is proportional to the real dynamic pressure. The variables b_1, b_2, q_c from Eqs. (4.1) and (4.2) are used to formulate a flow angle interpolation function f as defined in Eq. 4.3 using values from the calibration apparatus.

$$\xi = f(b_1, b_2) \qquad \xi = \alpha, \beta, \phi, \theta, A_{tot}, A_s \tag{4.3}$$

When employed in an unknown flow field Eqs. 4.4 and 4.5 are used to calculate the pressures. The angles $\alpha, \beta, \phi, \theta$ are obtained from the interpolation function f.

$$P_{tot} = p_i A_{tot}(b_1, b_2) q_c \tag{4.4}$$

$$P_s = P_{tot} - \frac{q_c}{A_s(b_1, b_2)} \tag{4.5}$$

The calibration is valid as long as the flow field during the calibration is representative of the unknown flowfield usage and the probe geometry is intact.

4.1.1 Uncoupled Single-Probe Setup

A graphical representation of a full cycle is shown in the flowchart in Fig. 4.2. The calibration process is marked with a green background and the measurement processes with a red background. Dashed lines and boxes indicate that new errors are introduced to the process. Most boxes and arrows have a general clarification of the processes or data being transmitted. Beginning with the calibration, the ambient flow properties are gathered together with probe port pressures. Uncertainty from the calibrator measurements and probe port pressures are introduced. These are later converted into dimensionless values using Eq. (4.1) and (4.2). This process called data reduction is, in this case, analytical, and does not add any uncertainty but can amplify them, as described in the following section. The dimensionless numbers and calibration values are used to formulate the interpolation function f. Later, when the measurements are sampled, uncertainties from port pressure measurements are introduced and once more the port pressures are converted into dimensionless number b_1, b_2. By the chosen algorithm, b_1, b_2 are interpolated using function f, which also introduces uncertainty. Flow angles are taken directly from the interpolation while dimensionless total and static coefficients need a scaling reference. This is achieved by using the quasi dynamic pressure q_c with the total and static pressure coefficient A_t and A_s as shown in Eqs. (4.4) and in (4.5). The calibration, data reduction and interpolation are described in detail at the next section using data from a calibration of a five-hole probe.

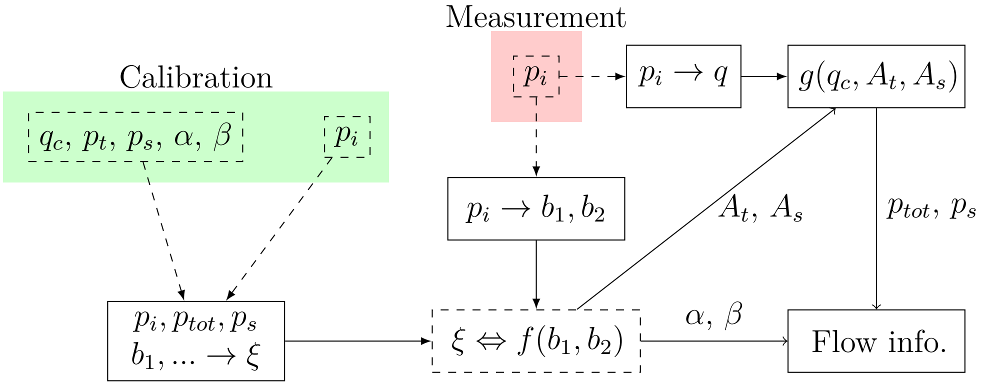

Figure 4.2: Flowchart of the multi-hole probe calibration and measurement process

4.1.2 Calibration

At the Chalmers Fluid and Thermal dynamics lab, the calibration is performed in a jet facility. The flow is powered by a centrifugal fan and the flow is straightened before entering the nozzle. Figure 4.3 shows the calibrator schematic with the flow from the left and probe pointing in from the right. The calibrated nozzle have an area ratio of four and the differential pressure over the contraction is monitored by a highly accurate micromanometer (FCO560) which measures the dynamic pressure in the jet. The pressure range of the FCO560 is 2000 Pa with an accuracy of 0.1% of the reading($0.1\%R$) with a $1.5e^{-6}$ full scale deflection (fsd). This method of specifying uncertainty is common in accreditation protocols but can be thought of as a scaled invariance statistical S_i random error and normal statistical bias error B_i, respectively. Errors are summed using root mean square(RMS) but, as shown later, it is beneficial to keep the statistical and random and bias error apart. A Prantl probe is added in the jet several probe diameters far from the probe for capturing of the total pressure and static pressure during the calibration. Temperature is measured with a PT-100 probe, with an uncertainty of ($0.02R + 0.1$ K). The reference probe and port pressures are measured with a digital multichannel pressure system PSI-9116 with 2.5 kPa pressure sensors mounted. The accuracy of the PSI-9116 is specified by the manufacturer as being 0.15% fsd. However, when calibrating against the FCO560 the uncertainty for the unit can be approximated by ($0.15\%R$, 0.15%fsd) or equivalent ($0.15\%R + 0.5$ Pa) in laboratory conditions.

In Fig. 4.3, centred around the probe is a schematic static pressure field. This is to illustrate the static pressure gradients found in the jet. Theoretically, the static pressure recovery after a jet nozzle should be instant. For most intents and purposes, this is indeed true as the pressure gradient found 30mm downstream the nozzle was in the order of 0.2% of the dynamic pressure per mm. However, this value is sufficiently large to affect the accuracy of the calibration. The nozzle coefficient has an estimated error of 0.06% from geometrical measurement. Attempts to further verify the nozzle were performed but the random noise from pressure transducers was a order of magnitude higher than expected error in the nozzle. The nozzle coefficient is used with the pressure difference from the contraction $q = \Delta Pk$. The traversing of the probe is done by two encoded brushless motors and the probe is

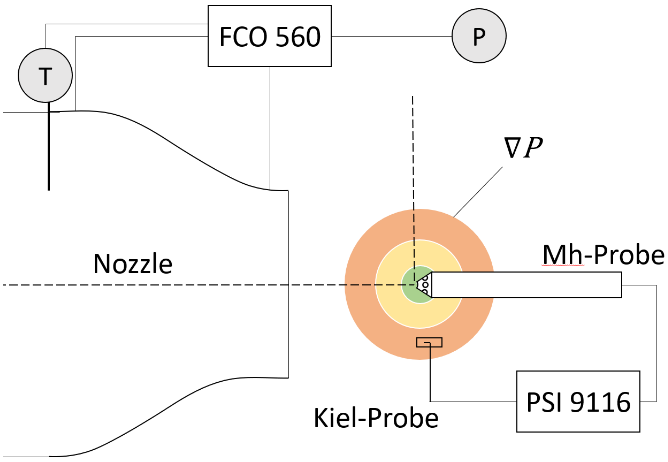

Figure 4.3: Schematics of Calibrator

manually aligned and oriented parallel in the nozzle flow. The position accuracy of the traverse system is significantly higher than the sensitivity of the probe so errors from this were neglected. A summary of the uncertainty for the equipment is shown in Table 4.1. The errors are divided into two rows: the first row shows the errors when some bias errors in the calibrator can be ignored, while the second row shows errors including bias errors from the calibrator. When using two probes that have been calibrated in the same calibrator, the upper row can sometimes be used. When using a single probe, the second row should be used. The values shown in Table 4.1 represent the values introduced in the green box in Fig. 4.2.

Table 4.1: Individual random and error for reference values during the calibration at a dynamic pressure of $q \approx 900$ Pa

	q	P_s	P_t	$\alpha + \beta$ [Deg]	P_i [Pa]	T [K]	P_{amb}
Cal	0.1R	0.4Pa	0.1R + 0.4Pa	0.03	0.15R + 0.5Pa	0.02	0.015
Abs	0.13R	0.9Pa	0.15R+ 0.9Pa	0.03	0.15R + 0.5Pa	0.1	0.2

4.1.3 Uncertainty from Data Reduction and Interpolation

As mentioned above, the propagation of errors need to be considered. A common way to achivie this is by using Eq. (4.6). To the best of the author's knowledge, this method was first formulated by [31] but is commonly used in standards such as ASME PTC 19.1 [4] or ISO 17025 [26]. The Taylor expansion can be used where the expression can be formulated analytically, the data can be assumed to be normally distributed and linear error predictions are reasonable. The dependable function is ς, x_i are the independent variables of the expression, and the error of each independent variable is represented by δ_{x_i}. All transducers are considered to be independent and the total error to be ε_ς.

$$\varepsilon_{\varsigma}(x_1, x_2, ..., x_n) = \left\{ \sum_{i=1}^{n} \left(\frac{\partial \varsigma}{\partial x_i} \cdot \delta_{x_i} \right)^2 \right\}^{1/2} \tag{4.6}$$

Utilising Eqs. (4.6), (4.1) and (4.2) provides the expected uncertainty when formulating dimensionless coefficient and reference data for interpolation. The Taylor expansion provides individual contributions from each independent variable to each dimensionless coefficient A_t, A_s, b_1, b_2, q_c.

An alternative method for uncertainty propagation estimation is to use Monte Carlo simulations(MCS). MCS [42] are empirical and can be utilised on black-box systems but do not, in general, provide the clear cause and effect that the Taylor series can. MCS can for most error estimation be generalised by Eq. (4.6). Perturbations δ are introduced on the average value x_i and introduced error on the function ς can be estimated as ε_{ς}. By introducing a significantly large population of perturbations, statistical assumptions can be used to estimate the uncertainty of the function ς.

$$\varepsilon_{\varsigma} = \varsigma(x_1, x_2, ...) - \varsigma(\widetilde{x_1}, \widetilde{x_2}, ...) \quad \widetilde{x_i} = x_i + \delta_i \tag{4.7}$$

Any statistical valid input can be used for perturbation. For this study, as very little information is known about the perturbations they are assumed to be Gaussian distributed. The probability distribution for PSI-9116 is relatively skewed as the bias error after re-zero is relatively large, at $0.4 - 0.6Pa$. This small offset has a small impact near the full scale, but at lower values can have a substantial effect. The same amplitude and variance are used for the Taylor series expansion and MCS. In Table 4.2 the uncertainty of the dimensionless coefficient is shown when using Taylor expansion on Eqs. (4.1) and (4.2).

Table 4.2: RMS of individual uncertainty at a dynamic pressure of $q \approx 900$ in the jet

	b_1	b_2	A_t	A_s	α	β	q
Cal	0.2%	0.19%	0.28%	0.1%	0.075	0.075	0.10
Abs	0.2%	0.19%	0.48%	0.3%	0.075	0.075	0.15

The interpolation function used in the thesis is a local linear interpolation scheme. The calibration is divided into local sectors depending on the maximum pressure port. Data from the neighbouring interpolations schemes are used when interpolation is performed along the boundaries of the sectors. The sector is chosen by the maximum port pressure. The sectoring is illustrated in Fig. 4.4a in relation to tip flow angles, the highest port number is written on the colour-coded sectors. Aerodynamic imperfections are usually shown by having non-symmetric sector distribution which is not found for this probe tip. The total pressure coefficient A_t for the sector with the center port perceiving the highest pressure is shown in Fig. 4.4b. The general parabolic shape of the coefficient relative to b_1 and b_2 is used in later discussions.

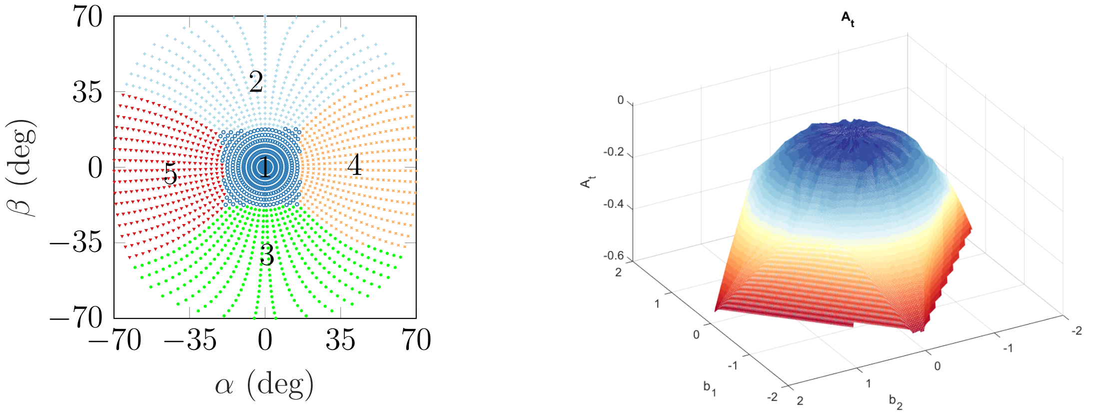

(a) Local interpolation scheme, each sector is marked with the highest pressure perceiving port

(b) Total Pressure coefficient A_t in sector one

Figure 4.4: Illustration of interpolation sectoring and total pressure coefficient at sector one.

If viewed carefully, there is some local noise at low b_1 and b_2, this is also discussed later.

In order to formulate a general expression for the uncertainty of an mhp the errors introduced from the interpolation function need to be defined or estimated. There have been extensive discussions regarding how to best estimate the errors in interpolation schemes, many that are connected to an ever-more complex data reduction model. These models are excluded as the main benefits from these relate to compressible effects or sparse calibration points, neither of which that are relevant to the work in this thesis. However, a summary of error estimations of interpolation methods is described below.

If the interpolation scheme is global, a common approach is to use the goodness of fit parameter, as utlilised by Crawford [16]. This, however, is not suitable for the local sectoring interpolation as used in this work. A less common method is to compare the calibration to the potential flow around a probe as performed by Ramakrishnan [37]. Data reduction and interpolation are also increasingly commonly replaced by neural networks, which show promising benefits. Uncertainty of this and traditional data reductions can also be estimated empirically using MCS. This was performed by Zilliac et al. [51], Johansen et al. [28] and Ghosh et al. [20]. Yasa et al. [48] subtracted single data-points along the interpolation dataset and analysed the effect this had on calibration to estimate the interpolation error.

In Papers 1, 3 and 4 of this thesis a mix of Taylor series and MCS has been implemented to estimate the interpolation error. Perez in [40] started by estimating the signal uncertainty using Taylor series and introducing these as a controlled perturbation on the interpolation function. By selecting the worst outcome the author should have obtained a very conservative uncertainty estimation. Less conservative approaches have been implemented gradually as confidence in the uncertainty method has increased.

The general rationale behind the uncertainty estimation is described below. Only effects on total pressure are shown but the method is valid for all quantities measured by the MHP. The linear validity of the linear approximation using Taylor series is evaluated against a MSC. This is performed by introducing the same perturbations for both Taylor series and MCS with a fixed calibration function. The results for such a comparison for a 2800 point calibration dataset are shown in Fig. 4.5. To ensure a statistical valid data set, 10,000 perturbations per data point were used for the MCS using the device accuracies specified in Table 4.1. In Fig. 4.5 a minor difference between the Taylor expansion and MCS results can be seen with the MCS predicting higher values. This is to be expected but the small difference indicates that the linearity of the Taylor series estimations are a decent estimate of the measurement uncertainty. At a cone angle of 20°, results from the MCS have a local maxium which is not captured by the Taylor series. This is primarily due to the high gradients of the total pressure coefficient found at these cone angles, as can be seen in Fig. 4.4. It is also the location where a sector change occurs and a small permutation can cause a jump between two sectors that introduce errors. Countering the effect from increased gradients is the RMS of the probe port pressures. Using potential flow, the port pressures of the probe become evenly distributed as the cone angle approaches half the probe geometrical tip angle. For this specific probe and conditions this occurs at $30 - 35°$. As the permutation scale against the port pressure the lowest RMS of the perturbation should be found in this location. From observing the results from the MCS, the effect from this seems to be small. This probe is nearly stalled at a cone angle of 45° and data above this are ignored.

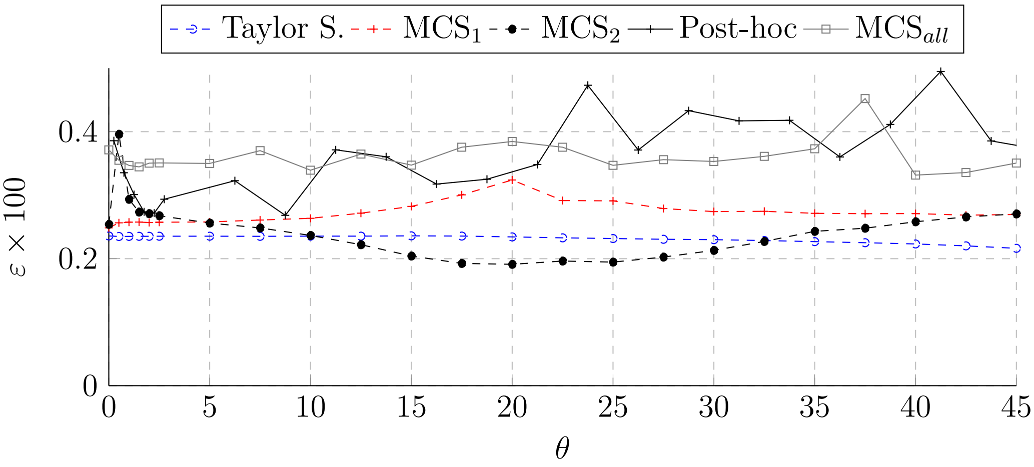

Figure 4.5: Comparison of estimations of using Taylor series, Monte Carlo simulations and a post-hoc error estimation check.

To evaluate and isolate the interpolation error, another MCS was performed including the effects from of the interpolation function. The results from this simulation are shown in Fig. 4.5 as a dashed black line and would be representative of a normal measurement but without uncertainty from the calibration procedure. A clear discrepancy can be found below cone angles of 2°, primarily due to the interpolation function for total pressure coefficient A_t is noisy at a low b_1 and b_2, as seen in Fig. 4.4b. Unexpected low values near a cone angle of $\approx 20°$ were observed. The only difference between the second and the first MCS is that the total pressure coefficient A_t is interpolated using the perturbed port pressures. From comparing the first and second MCS, the updated A_t seems to have a large effect near highest gradients of $A_t(b_1, b_2)$. This indicates that the contribution of interpolation has minor effects, except at very small cone angles for the investigated points. An interesting point is that the port pressure RMS is the same at a cone angle of $40 - 45°$ as $0 - 5°$ which is also very close to what is seen in second MCS.

As the perturbation during the second MCSs are centred around the calibration points, only a subset of the interpolation is evaluated. A a similar MCS was performed but utilising intermediate control points scattered in the space in between the calibration points, called the post-hoc dataset. This simulation produced near identical results to the previous one and is not shown in Fig. 4.5. This indicates that the resolution of the interpolation is sufficient and only small errors from the interpolation are to be expected.

A robust way to estimate the full system uncertainty under optimal conditions is to use control points measured post-hoc the calibration while using the identical conditions and equipment. The interpolation function from the earlier calibration is used on the post-hoc data-points which are compared to the measured quantities from the calibrator. This allows potential long-term bias errors on all transducers to be ignored as well as any probe alignment error. This primarily leaves relative uncertainty from transducers and interpolation error to contribute to any discrepancy between probe-measured and calibration reference values. The result from such a post-hoc error estimation is shown in Fig. 4.5 as a solid black line. There are notable similarities with the second MCS at low cone angles. The similarity near zero cone angle indicates that the estimated pressure perturbations are in the same order of magnitude. Finally, a MCS was performed for the whole system where perturbations are inserted at all measurement points and shown as greyed lines in Fig. 4.5. There are notable similarities with the post-hoc data even though MCS in general over-predicts the mean error. Above the first few points, the variance of the experimental post-hoc data is an order or magnitude higher compared to simulations. This is partly because of the large population size of the simulations but is also likely to be due to the Gaussian perturbation model as the lack of smaller random sensor biases are dampened in the simulations. There are also uncertainties in the post-hoc data that are not covered in the simulations or Taylor expansions. These are aerodynamic imperfections of the probe and uncertainties from the calibration process.

Without further investigation, a conservative estimation of the interpolation error is in the order of 0.15-0.25% for most of the dataset. As the interpolation error would be added using RMS the device uncertainty and data processing will contribute to a considerable larger part than interpolation. Take the example at near parallel flow: at this angle the centre port is dominant throughout the calibration and measurement. This can be seen in Eq. (4.2) and Eq. (4.3), with a high centre port pressure, this becomes dominant for both the total pressure coefficient A_t and q_c. The error introduced from the PSI-9116 would then be in the order of $\varepsilon P_t \approx \sqrt{\delta P_t + \delta P_t + \delta P_t} \approx 1.73 \delta P_t = 0.26\%$.

4.1.4 Measurement Considerations

When using a multihole probe there are a few considerations other than typical free-stream flow effects, such as viscous or compressible effect. First, a few specifics relevant to any pressure measurement using a pneumatic probe in flow measurement will be mentioned. i) It is intrusive and might change the flow field substantially. ii) The smallest feature you can resolve is the diameter of the port. As the ports on the MHP are distributed there is also the effect that any large gradient across the probe will lead to a difference between the measured and real incidence angles. Chernoray and Hjärne [13] presented a correction in high-gradient flow. As the probe is used in highly turbulent flow in the TRS and ICD, turbulence needs to be considered. Turbulence causes an overestimation of the measured port pressure. For an ideal case, this can be derived from a Reynolds decomposition of the Bernoulli equation as seen in Eq. (4.6) and introducing isotropic turbulence. By rewriting the expression to be dependent on turbulence and defined in $\sqrt{v'^2}/V = Tu$ an indication on the effect from turbulence can be estimated.

$$P_{tot} = P_s + 0.5\rho(V^2 + \langle u'^2 \rangle + \langle v'^2 \rangle + \langle w'^2 \rangle) = V^2(\sqrt{1 + 3Tu^2}) \tag{4.8}$$

The highest value of free-stream turbulence measured in the facility was 6%, which causes a 0.5% offset in measured total pressure. However, the turbulence downstream of the rotor is not isotropic. The effect of turbulence on MHP is still largely unknown, as stated by Tropera in [47]. Scribner [44] conducted an isolated study where no noticeable effect from turbulence below an intensity of 8% was found.

Large-scale fluctuations are present in the TRS, thus sample time must considered. This is case specific to each set-up and measurement point. Both Perez [40] and Axelsson [6] selected a few representative points and studied the effect of sampling time. As the uncertainties in MHP are highly dependent on the port pressure accuracy, this needs to be thoroughly studied for each new flow field.

4.1.5 Implementation in the TRS and ICD

For the data in attached papers, the TRS is instrumented with two MHP; one 5-hp to traverse the inlet boundary and one 7hp to study intermediate and outlet plane. In Fig.2.6 the general set-up and flowchart for processing pressure measurement are shown for the TRS.

With the definition of the error introduced in each sampling and processing step, an expression of the uncertainty in a measured point in the TRS was derived. The uncertainty of pressure perturbations on the calibration parameters was estimated using Taylor expansions as shown in Table 4.2 for the 5hp. The same methods was used with the measured data in the measurement plane. The uncertainties after data reduction are combined with an 0.2% interpolation error using RMS.

$$\varepsilon_{A_t} = \sqrt{(\varepsilon_{A_{t_{Cal}}})^2 + (\varepsilon_{A_{t_{Meas}}})^2 + (\varepsilon_{A_{t_{Interp}}})^2} \tag{4.9}$$

The error for the total pressure measured with the probe can now be written by using a Taylor expansion on Eq. 4.4 with δA_t provided from calibration. Turbulence is added using RMS. Figure 4.6a shows the total pressure on the outlet of the TRS at ADP and Reynolds Number of 235,000. Next to this, in Fig. 4.6, is the total pressure error for the same dataset.

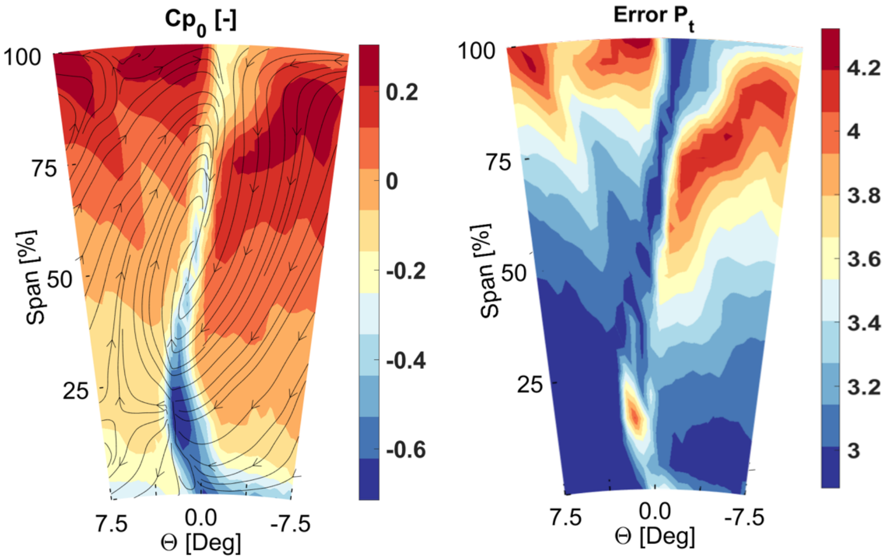

(a) Total pressure at the outlet plane of the TRS

(b) Estimated total pressure error using Taylor series at the outlet plane of the TRS at $Re = 465,000$

Figure 4.6: Outlet plane total pressure distribution with relative errors

As there is substantial turbulence decay throughout the TRS module the turbulence could cause a overestimation of the total pressure losses of near $0.5\%R$. This is relatively large as the mass flow average losses in the TRS is in the order of $1 - 5\%$. When operating at design conditions, both the ICD and the TRS have very small and localized total pressure losses. This makes inlet-outlet total pressure difference measurement challenging as the main losses come from thin wakes with large pressure gradients or separated flow, both of which are known to increase uncertainty in MHP measurements. The flow is also heavily redistributed leaving few areas for re-zero offset between the two boundaries.

4.1.6 Uncertainty Mitigation

In the TRS, the port pressure is one of the main contributors to the uncertainty in the pressure measurement. The uncertainty scales to port pressure; thus, if the RMS pressure of all the ports can be reduced so too will the introduced error. This is already implemented by using the room pressure instead of absolute values. However, in the TRS, room pressure might not be the best reference. A more appropriate reference might be values from the Prantle probe or another pressure source inside the TRS. The minimum transducer pressure range that can be utilised can be estimated by the static pressure coefficient.

Consider the flow around a semisphere with the free stream static as pressure reference to represent a multi-hole probe. The C_p value would be in the range of one to minus one, with some variations from losses and local acceleration/separations. At the stagnation point the value would be 1 with a values would be around $C_p - 1$ or lower on the acceleration peak. If instead, the total pressure in the free stream is used as the reference, the stagnation point will now have a pressure coefficient $C_p \approx 0$ while suction peak $C_p \approx -2$. In the ideal case, this would be worse for accuracy as you would need twice as large FS for the traducers in the second case compared with the first. In practice, transducers are available in set of ranges and the transducers in the TRS are used to ≈ 50% of FS at peak velocities. A conical multi-hole probe mounted in the TRS using the room pressure as a pressure reference has a pressure coefficient of $-1.6 \leq C_p \leq 1$ for angles up to cone angles of 70° and $-1.04 \leq C_p \leq 1$ for angles up to 45°. For increased accuracy the reference total pressure could then be implemented without risk of overloading the transducer. This has not been performed with the dataset presented in the attached paper but some version of this is used in the TRS and is expected to be implemented in the ICD. Estimated improvement by changing the reference pressure is illustrated in Fig. 4.7 using the same data set as used in Fig. 4.5. The blue curve shows a MCS of the method implemented in attached papers and the red shows a MCS when using the total pressure as reference. The introduced perturbations include a bias offset with the properties $0.15\%R + -0.6Pa$.

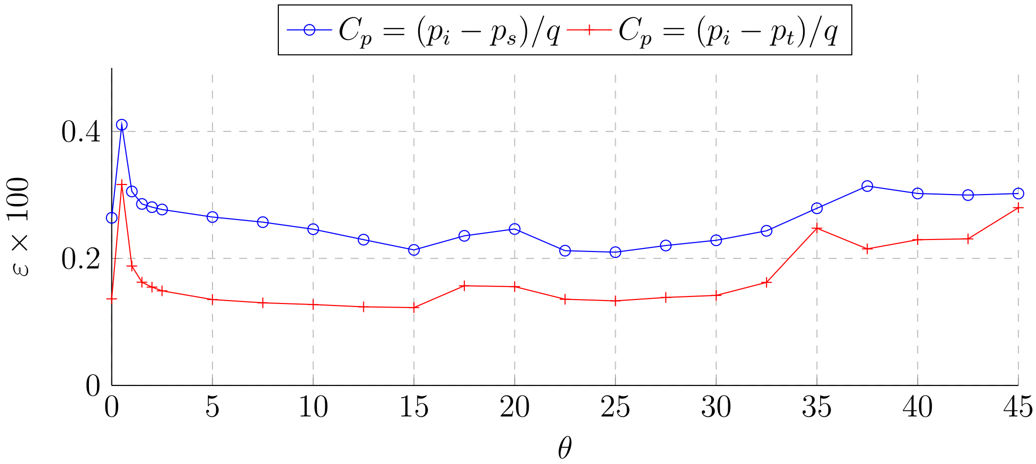

Figure 4.7: Comparison of the effect of changing pressure reference to the mhp, using MCS to estimate the effect

Figure 4.7 shows that there is a substantial gain in accuracy of total pressure measurement to be had when changing the reference in TRS. The potential gain in the ICD has to be investigated when implemented.

4.2 Heat Transfer using IR-Thermography

In project A3TE, measures were to be taken to improve the accuracy and preferably make steady state heat transfer measurement more cost effective. This was to enable -"the most comprehensive experimental data set of the TRS module" - AT3E project description. During the maturing of this system transient methods where also implemented.

The aim for the implementation of the IR-thermography was to measure the convective heat flux coefficient h_2 as defined in Eq. (4.10). In Eq. (4.10), convective heat flux is represented by q''_{conv}, surface temperature by T_w and free stream air temperature as T_∞. As surface temperatures are measured using IR-thermography this chapter focuses only on methods utilising this technique.

$$q''_{conv} = h_2(T_w - T_\infty) \tag{4.10}$$

At first glance Eq. 4.10 looks uncomplicated. However, in comparison to other measurement techniques used in the Chalmers Laboratory of Fluids and Thermal Sciences, heat transfer measurements have in general a significantly lower acceptable confidence level. This is partly due to the multidisciplinary nature when implemented, from the humidity impact on material properties to radiative interactions that can have effects up to $20\%R$. To enable heat flux measurement, there must be a heat flux, which can be achieved by artificially warming or cooling the surface. The delivery method does theoretically not matter. However, below is a short summary of methods often used together with IR-thermography as measurement can be achieved with reasonable accuracy.

A solid core is heated with a polymer or ceramic isolation, and the heat flux through the isolation layer can be measured by the temperature difference. This method has been successfully implemented by Osso [2] et al. in a intermediate compressor duct. The main disadvantage is the uncertainty in the thermal contact resistance between the isolating shell and the core and isolation shell thickness variations. A small air pocket can increase the thermal contact resistance by an order of magnitude. Uniform isolation is also challenging to achieve cost effectively. However, the methods is very robust and if these two factors can be mitigated, it can be considered a very suitable method.

Electric heating via resistance can be utilised, this was implemented by Wang [50] in an linear cascade and as by Johansson [29] in a intermediate turbine duct. Foils can be used alone or glued on a geometry can via electric resistance provide a heat flux with an approximated best-case scenario of non-uniformity of around $1 - 3\%$ [5]. However, this method is not suitable for double curved surfaces such as thoes found on the OGV. The effect of two-directional bending the element changes the resistance, thickness, or might break the heater completely. Minor bends are possible, for example by vacuum moulding the foils on the model, but it is likely that the uniformity of the heating would be compromised. Another issue is the electric resistance dependency of temperature causing a non-uniform input flux where a large local difference in temperature can be found. To the best of the author knowledge, a high accuracy achieved using this method on a high curvature model is $10 - 13\%$ as shown by Povey [14].

A liquid hot core uses circulating internal hot liquid to provide a heat flux through an isolating layer. This provides a high degree of freedom for the designer as the liquid can be transported where it is needed and very thin passages can be reached. The main challenge is the thermal resistance of the isolation, the thermal resistance on the liquid side of the isolation and the material interaction with the liquid when using polymers to create the isolation. There are also high risk of leaks.

Radiation/Induction can both be used to provide a steady heat flux to the surface or test body. This a very useful technique as the test object does not need any instrumentation. A key challenge when performing steady state heat transfer is to quantify heat flux from the radiation/induction. Another usage of radiation/induction is to heat up objects and study at the temperature decay as the heating source is removed. With this method accuracy scale to the temporal resolution and high sensory throughput is still very expensive in the IR-spectrum, although this is rapidly changing.

Each method was evaluated and benchmarked for calculated accuracy and price. This was performed using simple error estimations with one-dimensional approximation and Taylor series and MCS for error propagation. All independent variables were assumed to have a normal distribution. A comprehensive uncertainty analysis of the liquid core method is presented in Paper 4 and using transient heat flux measurement is currently under investigation. A short description of the implementation in the TRS and a summary of the uncertainty analysis is given below.

4.2.1 Steady State Heat Transfer

The steady state convective heat transfer measurement performed in this work is achived by manufacturing a plastic model by stereo lithography(SLA) with internal water channels. In the water channels, hot water is circulated, which acts as a uniform temperature inner core. The plastic model acts as an insulation layer around this warm core. The temperature difference between the core and the outside air flow causes a heat flux through the isolating shell. From the surface temperature of the isolation the conductive heat flux through the wall can be calculated. The conductive heat flux through the wall is transported away by radiation and convection into the outside air. As interest is paied to the convective part, the radiative part needs to be isolated or minimised. The measurement or estimation of the radiative part is often the most arduous part of the problem but was made possible by using a modified version of the RMA method as formulated by Kirollos [30]. Figure 4.8 shows the general setup of the measurement with the accompanied main thermal fluxes defined in Eqs. 4.11 to 4.13. To the left is an instrumented vane and to the right is a one-dimensional representation of a cut-out section of the OGV wall. Pink arrows symbolise heat fluxes. There are four indexed positions. Variables that are sub-indexed with 1 represent the inner wall values; this is the wall temperature T_1, inner wall heat transfer coefficient h_1 and average water temperature T_1^∞. Sub-index 2 is used for surface properties, such as temperature T_2 and emissivity ε_2. As the surface consists of two types of treatment, both gold $\varepsilon_{2,1}$ and a black Nextel paint, ε_2 the sub-index $2,1$ is used for the gold-leaf markers. Sub-index 3 is for air properties

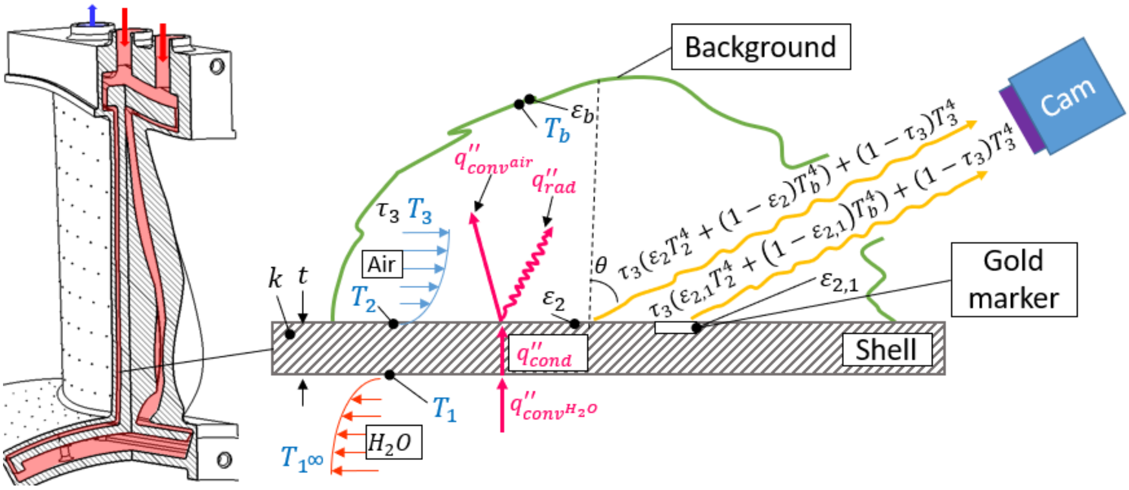

Figure 4.8: Schematics of the instrumented heat transfer OGV together with a one-dimensional simplification

and group b is for background properties. σ is the Stefan – Boltzmann constant, t is the shell thickness and k thermal conductivity.

$$q''_{cond} = \frac{k}{t}(T_1 - T_2) \tag{4.11}$$

$$q''_{conv^{H_2O}} = h_1(T_{1\infty} - T_1) \tag{4.12}$$

$$q''_r \approx \sigma\left(\varepsilon_2 T_2^4 - \tau_3 \varepsilon_b T_b^4\right) \tag{4.13}$$

Using conservation of energy with Eqs. 4.10 to 4.13 and solving for convective heat transfer coefficient on the air side h_2 provides Eq. 4.14.

$$h_2 = \frac{q''_{cond} - q''_r}{(T_2 - T_3)} = \frac{1}{(T_2 - T_3)}\left(\frac{k}{t}(T_1 - T_2) - \sigma\left(\varepsilon_2 T_2^4 - \varepsilon_b T_b^4\right)\right) \tag{4.14}$$

Note that most variables in Eq. 4.14 are highly dependent on test conditions and seemingly uncoupled variables are coupled by these dependencies. The effects of this need to be carefully considered when designing for heat transfer studies. For example, the thermal conductivity of the wall changes with temperature and ambient humidity among others $k = f(T, RH, ...)$. The thickness is dependent on the thermal expansion coefficient $t = \alpha(T)$. Emissivity is temperature dependent, the optical transmission of air is strongly dependent on the amount of moisture in the air which is dependent on air temperature, etc. From a practical point of view, the effect from this needs to be estimated so that either they can be accounted for, mitigated, or neglected. To a large extent, this has been performed in Paper 3.

Measurement Procedure

Figure 4.9 shows the data flow and processing when performing a surface temperature measurement and general steps to calculate the heat transfer coefficient h_2. The green area marks the calibration procedure. The red areas mark the measurement processes to the point where reliable surface and background temperature have been defined. The red box External is external material and geometrical errors which are included in the error estimation. Errors introduced outside the coloured areas are from such issues as geometrical translations or FEM calculations which are not included here. Before measurements, the camera counts X are correlated to surface temperatures, view angles θ, focal settings, etc. This is saved as a non-uniformity compensation(NUC) and a polynomial function. When the camera is used during measurement, the counts are converted to surface temperature $T_2, T_{2,1}$. As the camera sensor is sensitive to the temperature of the optics and the temperature of the surrounding air an in-situ correction is applied using a PT-100 temperature sensor which is coated in the same material as the test object, T_{is}. Firstly, the heat transfer coefficient h_2 is calculated assuming one-dimensional wall behaviour and T_2 as surface temperature. Later, the effective wall temperature T_w and the effective background T_r temperature are calculated using the RMA method. One dimensional heat transfer coefficient is calculated again using T_w and T_r to evaluate the effect from the RMA method. The temperature images are mapped to real world coordinates(RWO) using gold markers on the surface of the OGV. As several fields-of-view are necessary to capture the vane heat transfer the data is normalised and merged. Following this, FEM simulations are used with surface, ambient and core temperatures to capture the in-wall heat flux. Finally, the heat transfer coefficient can be presented. Below an attempt is made to estimate the errors introduced in the spatial conversion of images, data normalisation and FEM calculations. Note that these are rough estimations. One method is to use the one-dimensional results as a reference. The potential error can be estimated by order of magnitude of the effect the process has on the reference data. When comparing the final h_2 using FEM to the one-dimensionally calculated h_2, discrepancies found near the suction side transition was in the order of $1 - 2\%$. The maximum difference between FEM and one-dimensional calculations differs by 3%, which was found near the hub at the suction side. The errors introduced from the FEM calculations are hence expected to be negligible. Even with a unlikely 50% error from the FEM calculation would still be shadowed by measurement error if summed by RMS. The errors introduced from mapping the image to real world coordinates cannot be estimated using this method.

Figure 4.10 shows an example of the process. On the left is a photo of the OGV coated with Nextel paint and gold markers. The next is the surface temperature T_2 shown after the markers have been filtered out. The results from the RMA method where the effective background temperature T_r and surface wall temperature T_w are shown. To the right is an isometric view of the FEM implementation with a detailed view of the mesh.

4.2.2 Transient Heat Transfer

The data used for heat flux transfer measurement in the LPT-OGV rig have large temporal variation and average values of 500-1000 images was used to mitigate statical uncertainty. There are two types of noise sources: the first is the noise in the data acquisition system, the second is due to the unsteady nature of the flow

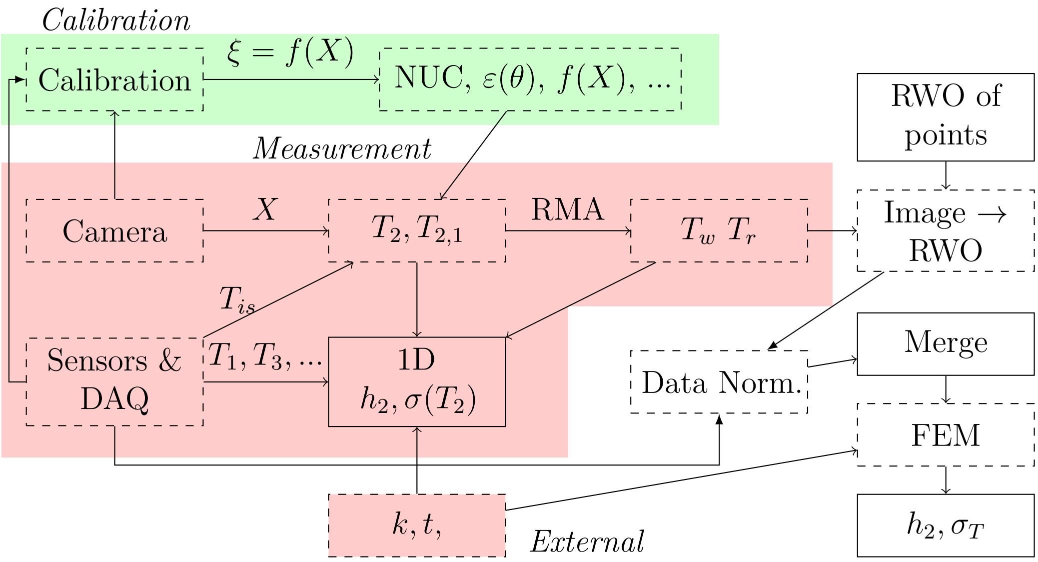

Figure 4.9: Steady state heat transfer measurement flowchart. Dashed boxes illustrate introduced error in the process

field which causes locally increased or reduced cooling. Some of these flow features can be separated from the random noise of the data acquisition.

There are limits to what kind of features can be detected based on the thermal capacity of the surface, camera noise levels and camera time resolution. The capacity of the surface can either delay or completely dampen away features that are either too short-lived or too weak to cause sufficient cooling effect. The camera background noise referred to as Noise Equivalent Temperature Difference(NETD) and is, in better cases, around 10-20mK. The maximum full-frame sample frequency for measurement around room temperature is around 1kHz for a camera such as the FLIR X6900sc but is only 120hz for the Phoenix 320.

The processing of this transient data can be performed in the time or frequency domain. In the time domain the surface temperature surface standard deviation σ_T is commonly used to detect steady transition and separation streaks as these contain high levels of unsteady flow. On the attached flow such as a two-dimensional airfoil of a flat plate an increase in σ_T would signify a laminar-turbulent transition,

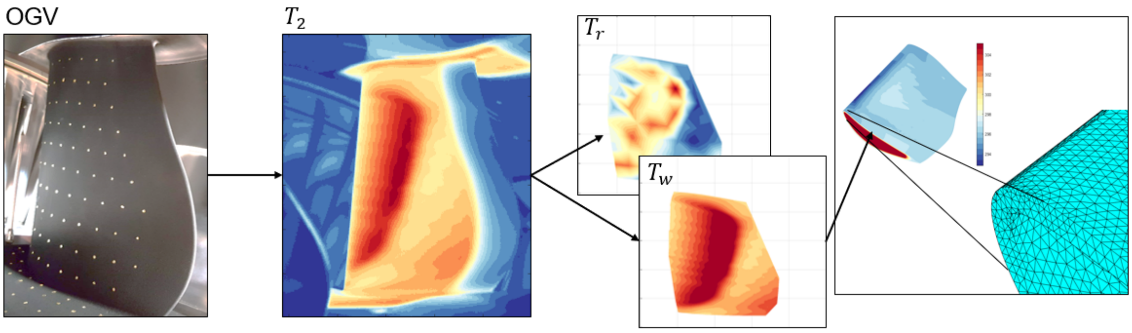

Figure 4.10: Processing of average IR-Thermography data

as shown in [39]. In separated flow the σ_T are as a rule higher then in transition as shown by [38]. An example of transition in the TRS can be seen as peak σ_T in Fig. 4.11a marked with A. When increasing the blade loading as in Fig. 4.11b a corner separation can be seen with higher σ_T marked as A. Some features such as roll-up vortex have a sufficient cooling effect to be detected using this configuration, marked as B in Fig. 4.11a. In Fig. 4.11c, the sliding frame subtraction(SFS) is able to capture individual streaks and transient features on the surface, but with the Phoenix 320 camera at 120Hz the time resolution is insufficient to provide much more data than σ_T. The methods mentioned above are often referred to as differential IR-thermography(DIT) since [36] formulates this expression.

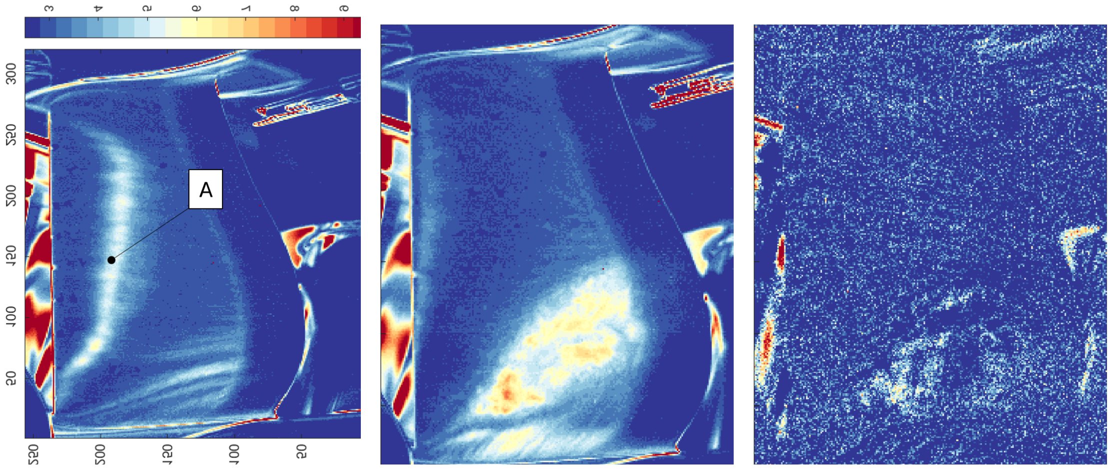

(a) σ_T at ADP (b) σ_T at ADP+15 (c) SFS at ADP+15

Figure 4.11: σ_T transition and separation comparison at $r \times 10^{=,235,000}$ with different load factors

In Paper 4 this technique to detect transition is verified at midspan on the suction side of an OGV. The location of the roll-up vortex is in agreement with oil visualisation.

Chapter 5

Summary of Papers

Paper 1

Division of Work

Besides being the main author, my main contribution is the experimental implementation and analysis. The co-authors provided feedback on the paper and findings in the work.

Summary and Discussion

This paper presents novel results of surface roughness and Reynolds effect on the losses on the TRS. Three different levels of roughness are applied and tested at design conditions at two different Reynolds numbers. The two surface roughnesses with lowest the Ra are in the range of what would be reasonable to assume is in a TRS module during real engine conditions. Since the effect from the surface roughness was unknown at the start of the experiment a sample with very high surface roughness $Ra \approx 30$ was added to emphasise the effect of surface roughness variation. Turbulence decay and pressure-based boundary layer measurement was performed. Suction side surface features were documented via flow visualisation.

As two Reynolds numbers were tested the Reynolds effect could be seen for both a hydraulic smooth vane as well as the rough surfaces. Flow visualisation also showed the secondary flow structure and estimated transition/separation area along the section side.

At low Reynolds numbers the experimental results follow typical surface roughness where an increased surface roughness causes an incrementally increased wake width and losses along the whole span. At higher Reynolds numbers the effect was the same for the two first samples but for the roughest surface there was a substantial increase of losses focused around the suction side near the hub.

Contribution

This was the first to paper to present roughness effects in an annular TRS module. The paper also provides reference values for numerical studies to verify for turbulence decay, Reynolds effects as well as roughness effects. Moreover, flow visualisation and boundary layer identified critical areas for further experimental studies.

Paper 2

Division of Work

Apart from being the main author, I provided conceptualisation, measurement and data analysis. Valery Chernoray contributed with conceptualisation and feedback on findings and Radeshee Dhanasegaran provided support with experimental measurement and set-up as well as writing.

Summary and Discussion

This paper is primarily a description of the uncertainty estimation and mitigation for steady state heat transfer when implemented in the TRS. The heat transfer coefficient distribution reveals the same surface features from flow visualisation as seen in Paper 1 with a similar sized roll-up and transition/separation location.

Contribution

The paper presents the first heat transfer measurement on a TRS at engine-representative conditions. Additionally, a very accurate and relative easy implementation of heat transfer studies was presented. The method has very little geometrical limitations and is suitable for many fields and problems. The paper is not a complete guide but shows how to mitigate most of the uncertainness often found in heat transfer studies.

Paper 3

Division of Work

As a second author of this paper I primarily provide experimental data and analysis but also feedback on the numerical findings presented. Shrikanth Deshpande performed the numerical study and the writing. Valery Chernoray provided feedback on the findings.

Summary and Discussion

The paper reported a numerical analysis of the experimental study performed in Paper 1. This was achieved by using steady state RANS simulations with a correlation-based transition SST model ($\gamma - \theta$). Since no information about the boundary layer moment thickness at the transition location was known the default settings of the transition model were used.

Contribution

Both wake studies and blade loadings are used to compare numerical and experimental data with good agreement. The losses are in general overpredicted in the numerical case but underestimated the relative increase in losses found with increased surface roughness.

Paper 4

Division of Work

Besides being the main author, I provided the experimental analysis and results. Boundary layer measurement using hotwire was taken from a subset in and dataset of unpublished work by Valentin Vikhorev. Srikanth Deshpande performed the numerical studies while Jonas Larsson and Oskar Thulin provided valuable analysis and support in writing. Valery Chernoray provided general feedback and help with data sampling of the hot-wire measurement.

Summary and Discussion

The paper primarily covers three aspects. Firstly it discusses in detail the usage of IR-thermography for full-span transition measurement on the suction side. Secondly the transition modelling on an hydraulic smooth vane is studied and compared in detail at midspan transition location and in general across the whole span. Finally fundamental transition correlations are compared to experimental and numerical findings.

Contribution

First, the paper provides for the first time a full-span transition measurement on the suction side on the OGV. The experimental results are compared to numerical data. The numerical simulation predicts an early transition across the whole span and the discrepancy increases with blade loading. Both numerical and measured transition momentum thickness Reynolds number agree with correlation at midspan. Streamlines give more insight into the increased losses observed in numerical simulations of the TRS as the blade loading increases.

Chapter 6

Concluding Remarks

The main aim of the thesis is to study and develop methods for experimental aerothermal investigation in turbine rear structures and intermediate compressor ducts in turbomachinery. Method development in a lab is a continuous process, and the main contribution from this thesis is listed below.

1. The multihole probe has been thoroughly studied for implementation in the TRS module. Chapter 4 shows the substantial work behind the uncertainty estimation for the data presented in Paper 1, 3 and 4. The findings show that with the current data reduction model and the ones that the author is aware of, the main contributor to measurement uncertainness is the pressure transducer used for the pressure probe. Even though extensive error analysis and mitigation have been performed, the accuracy is still insufficient to provide mass-flow averaged losses in the TRS module with high confidence. One improvement to mitigate uncertainties is presented where the reference pressure for the transducer is adopted for total pressure measurement. The same approach can be applied for any probe set-up.

2. The uncertainty in heat transfer measurement using a liquid core has in large part been quantified and evaluated. The uncertainty analysis shows the method is in the upper region for similar heat transfer studies. There is still potential uncertainty in humidity to the thermal conduction of the insulation but these has, to the best of the author's best knowledge, not be included by any earlier experimental heat transfer study. Errors from data normalisation and FEM calculations are not included but these should in not introduce any errors in the order of magnitude as the measurement data.

3. All the instrumented vanes are manufactured by the additive manufacturing SLA. There are very few geometrical limitations and the method can easily be implemented for most other studies. However, when designing the experiment, wall thickness and inner wall liquid velocity need to be adjusted to suit the expected heat transfer rate on the airside.

4. Transition detection using IR-thermography has been verified using boundary layer hot-wire. IR-thermography can thus be used to trace transition location in the TRS.

Future Work

For the author, the main effort in the near-future work is to commission the new compressor facility in ENABLEH2 project. Concurrently, there is ongoing work related to both presented heat transfer and multi-hole probe. Firstly, minor adoptions are needed to implement the techniques mentioned in this thesis for the new compressor facility. Secondly, with ongoing development we hope to achieve capabilities beyond the state-of-the-art. There is an endless list of potential future work related to the measurement in the TRS and ICD, a selection of which is provided below. The fluid core heat transfer measurement method should be evaluated against analytical and fundamental cases to verify the existing and residual assumptions mentioned in Paper 2. The proposed reference offset in the TRS should be evaluated and a new uncertainty estimation performed for this experimental data. The introduction of the new SLS cameras in the IR-spectrum with higher sensitivity and lower integration time, enables useful frequency analysis of the surface temperature. This new technology should utilised in future transient heat transfer studies.

Bibliography

[1] B. J. Abu-Ghannam and R. Shaw. “Natural Transition of Boundary Layers—The Effects of Turbulence, Pressure Gradient, and Flow History”. In: *Journal of Mechanical Engineering Science* 22.5 (1980), pp. 213–228.

[2] Carlos Arroyo Osso, T. Gunnar Johansson, and Fredrik Wallin. “Experimental Heat Transfer Investigation of an Aggressive Intermediate Turbine Duct”. In: *Journal of Turbomachinery* 134.5 (May 2012). ISSN: 0889-504X.

[3] ASME ASME International. *Flow Measurement PTC 19.5*. Tech. rep. ASME International ASME, 2004.

[4] ASME ASME International. *Test Uncertainty PTC 19.1*. Tech. rep. ASME International ASME, 2005.

[5] T Astarita et al. “A survey on infrared thermography for convective heat transfer measurements”. In: *Optics & Laser Technology* 32.7 (2000). Optical methods in heat and fluid flow, pp. 593–610. ISSN: 0030-3992.

[6] Lars-Uno Axelsson. *Experimental investigation of the flow field in an aggressive intermediate turbine duct.* Doktorsavhandling vid Chalmers tekniska högskola Ny serie: 2945. Chalmers University of Technology. ISBN: 9789173852647.

[7] D. W. Bailey et al. “Performance Assessment of an Annular S-Shaped Duct”. In: *Journal of Turbomachinery* 119.1 (Jan. 1997), pp. 149–156.

[8] KW Barker, RW Gallington, and SN Minister. *Calibration of Five-Hole Probe for online Data Reduction.* Tech. rep. USAFA-TR-79-7, 1979.

[9] J.B. Barlow, W.H. Rae, and A. Pope. *Low-Speed Wind Tunnel Testing.* Aerospace engineering, mechanical engineering. Wiley, 1999. ISBN: 9780471557746.

[10] P. Bradshaw and R.C. Pankhurst. “The design of low-speed wind tunnels”. In: *Progress in Aerospace Sciences* 5 (1964), pp. 1–69. ISSN: 0376-0421.

[11] K.M. Britchford et al. “Measurement and prediction of low in annular S-shaped ducts”. In: *Experimental Thermal and Fluid Science* 9.2 (1994). Special Issue on Measurement in Turbulent Flow, pp. 197–205. ISSN: 0894-1777.

[12] Shaowen Chen et al. “Numerical Study of the Air Bleeding Caused Non-Uniformity in Axial Compressor”. In: *Journal of Thermal Science* 29 (Mar. 2019).

[13] Valery Chernoray and Johan Hjärne. “Improving the Accuracy of Multihole Probe Measurements in Velocity Gradients”. In: 2 (Jan. 2008).

[14] Matthew Collins, Kam Chana, and Thomas Povey. "Improved Methodologies for Time-Resolved Heat Transfer Measurements, Demonstrated on an Unshrouded Transonic Turbine Casing". In: *Journal of Turbomachinery* 138.11 (May 2016).

[15] James Crawford and A Michael Birk. "Improvements to common data reduction and calibration methods for seven hole probes". In: *Journal of fluids engineering* 135.3 (2013).

[16] James Crawford and A. Michael Birk. "Improvements to Common Data Reduction and Calibration Methods for Seven Hole Probes". In: *Journal of Fluids Engineering* 135.3 (Mar. 2013). ISSN: 0098-2202.

[17] N. Andersson E. M. V. Siggeirsson and M. O. Burak. "Numerical and Experimental Aerodynamic Investigation of an S-shaped Intermediate Compressor Duct with Bleed". In: *Accepted for publication in Journal of Turbomachinery (2020)* (2020).

[18] KN Everett, AA Gerner, and DA Durston. "Seven-hole cone probes for high angle flow measurement Theory and calibration". In: *AIAA Journal* 21.7 (1983), pp. 992–998.

[19] Karen A. Flack and Michael P. Schultz. "Review of Hydraulic Roughness Scales in the Fully Rough Regime". In: *Journal of Fluids Engineering* 132.4 (Apr. 2010). ISSN: 0098-2202.

[20] A. Ghosh, D. M. Birch, and O. Marxen. "Neural-Network-Based Sensor Data Fusion for Multi-Hole Fluid Velocity Probes". In: *IEEE Sensors Journal* 20.10 (May 2020), pp. 5398–5405. ISSN: 1558-1748.

[21] Johan Groth and Arne V Johansson. "Turbulence reduction by screens". In: *Journal of Fluid Mechanics* 197 (1988), pp. 139–155.

[22] *Some Effects of Non-Axisymmetric End Wall Profiling on Axial Flow Compressor Aerodynamics: Part I—Linear Cascade Investigation.* Vol. Volume 6: Turbomachinery, Parts A, B, and C. Turbo Expo: Power for Land, Sea, and Air. June 2008, pp. 543–555.

[23] Johan Hjärne, Valery Chernoray, and Jonas Larsson. "Experimental Investigations and Numerical Validation of an Outlet Guide Vane With an Engine Mount Recess". In: *Proc. of ASME Turbo Expo 2008.* June 2008, pp. 989–998.

[24] Johan Hjärne, Valery Chernoray, Jonas Larsson, et al. "Numerical validations of secondary flows and loss development downstream of a highly loaded low pressure turbine outlet guide vane cascade". In: *Proc. of ASME Turbo Expo 2007.* 2007, pp. 723–733.

[25] Johan Hjärne, Jonas Larsson, and Lennart Lofdahl. "Performance and Off-Design Characteristics for Low Pressure Turbine Outlet Guide Vanes: Measurements and Calculations". In: *Proc. of ASME Turbo Expo 2006.* Vol. Volume 6: Turbomachinery, Parts A and B. May 2006, pp. 649–658.

[26] ISO International Organization for Standardization. *General requirements for the competence of testing and calibration laboratories, 17025.* Tech. rep. International Organization for Standardization, 2008.

[27] ISO International Organization for Standardization. *Geometrical Product Specifications (GPS) — Surface texture, 4287.* Tech. rep. International Organization for Standardization, 1997.

[28] Espen S. Johansen, Othon K. Rediniotis, and Greg Jones. “The Compressible Calibration of Miniature Multi-Hole Probes ”. In: *Journal of Fluids Engineering* 123.1 (Sept. 2000), pp. 128–138. ISSN: 0098-2202.

[29] Martin Johansson. “Aerothermal Study of Intermediate Turbine Ducts”. PhD Thesis. Gothenburg: Chalmers University of Technology, 2016.

[30] B Kirollos and T Povey. “High-accuracy infra-red thermography method using reflective marker arrays”. In: *Measurement Science and Technology* 28.9 (2017), p. 095405.

[31] H.H. Ku. “Notes on the use of propagation of error formulas”. In: *Journal of Research of the National Bureau of Standards* 70C.4 (1966), p. 263.

[32] Andreas Marn et al. “Comparison of the Aerodynamics of Acoustically Designed EGVs and a State-of-the-Art EGV”. In: 45608 (2014).

[33] Robert Edward Mayle. “The 1991 IGTI Scholar Lecture: The Role of Laminar-Turbulent Transition in Gas Turbine Engines”. In: *Journal of Turbomachinery* 113.4 (Oct. 1991), pp. 509–536. ISSN: 0889-504X.

[34] F. R. Menter et al. “A Correlation-Based Transition Model Using Local Variables—Part I: Model Formulation”. In: *Journal of Turbomachinery* 128.3 (Mar. 2004), pp. 413–422.

[35] T. J. Praisner and J. P. Clark. “Predicting Transition in Turbomachinery—Part I: A Review and New Model Development”. In: *Journal of Turbomachinery* 129.1 (Mar. 2004), pp. 1–13.

[36] Markus Raffel and Christoph B Merz. “Differential infrared thermography for unsteady boundary-layer transition measurements”. In: *AIAA journal* 52.9 (2014), pp. 2090–2093.

[37] Vijay Ramakrishnan and Othon Rediniotis. “Calibration and Data-Reduction Algorithms for Nonconventional Multihole Pressure Probes”. In: *Aiaa Journal - AIAA J* 43 (May 2005), pp. 941–952.

[38] Kai Richter et al. “Boundary layer transition characteristics of a full-scale helicopter rotor in hover”. In: *AHS 72nd Annual Forum.* 2016, pp. 17–19.

[39] Kai Richter et al. “Detection of Unsteady Boundary Layer Transition Using Three Experimental Methods”. In: Jan. 2016.

[40] Borja Rojo. “Aerothermal Experimental Investigation of LPT-OGVs”. PhD Thesis. Gothenburg: Chalmers University of Technology, 2017.

[41] Borja Rojo, Carlos Jimenez, and Valery Chernoray. “Experimental Heat Transfer Study of Endwall in a Linear Cascade with IR Thermography”. In: *EPJ Web of Conferences* 67 (Feb. 2014).

[42] Reuven Y. Rubinstein and Dirk P. Kroese. *Simulation and the Monte Carlo method.* Wiley series in probability and statistics. John Wiley & Sons, 2017. ISBN: 9781118632161.

[43] Hermann Schlichting and Klaus Gersten. *Boundary-Layer Theory.* Berlin, Heidelberg: Springer Berlin Heidelberg, 2017.

[44] Carmen Andrew Scribner. “The Effect of Turbulence Intensity and Reynolds Number on the Aerodynamic Behaviour of Kiel, Three-Hole, and Seven-Hole Pressure Probes”. MA thesis. 1125 Colonel By Dr, Ottawa, ON K1S 5B6, Kanada: Carleton Universityn, 2011.

[45] Loris Simonassi et al. “On the influence of an acoustically optimized turbine exit casing onto the unsteady flow field downstream of a low pressure turbine rotor”. In: *Journal of Turbomachinery* 141.4 (2019), p. 041003.

[46] James V. Taylor and Robert J. Miller. “Competing Three-Dimensional Mechanisms in Compressor Flows”. In: *Journal of Turbomachinery* 139.2 (Oct. 2016). ISSN: 0889-504X.

[47] Cameron Tropea and Alexander L Yarin. *Springer handbook of experimental fluid mechanics.* Springer Science & Business Media, 2007.

[48] Laura Villafañe and Guillermo Paniagua. “Aerodynamic impact of finned heat exchangers on transonic flows”. In: *Experimental Thermal and Fluid Science* 97 (2018), pp. 223–236. ISSN: 0894-1777.

[49] *Numerical Design and Experimental Evaluation of an Aggressive S-Shaped Compressor Transition Duct With Bleed.* Vol. Volume 7: Turbomachinery, Parts A, B, and C. Turbo Expo: Power for Land, Sea, and Air. June 2011, pp. 151–161.

[50] Chenglong Wang et al. “An experimental study of heat transfer on an outlet guide vane”. In: *ASME Turbo Expo 2014: Turbine Technical Conference and Exposition.* American Society of Mechanical Engineers Digital Collection. 2014.

[51] GG Zilliac. “Modelling, calibration, and error analysis of seven-hole pressure probes”. In: *Experiments in Fluids* 14.1-2 (1993), pp. 104–120.